

# Gas Distribution and Starburst Activity in the Widely Separated Interacting Galaxies NGC 6670

Wei-Hao Wang<sup>1,4</sup>

wang@ifh.hawaii.edu

K. Y. Lo<sup>1</sup>

kyl@asiaa.sinica.edu.tw

Yu Gao<sup>2</sup>

gao@ipac.caltech.edu

and Robert A. Gruendl<sup>3</sup>

gruendl@astro.uiuc.edu

## ABSTRACT

We present high resolution H I 21 cm line, 20 cm radio continuum, and CO(1–0) line observations of the luminous infrared galaxy NGC 6670. NGC 6670 consists of two edge-on disk galaxies (NGC 6670E and NGC 6670W) with a projected nuclear separation of  $\sim 16$  kpc. While there are no optically identified tidal features and the molecular disks are not distorted much, we have detected a 90 kpc long H I tail which suggests that the galaxies are interacting and have already experienced at least one close encounter. The galaxies appear to be gravitationally bound and in a prograde-prograde orbit, which is the most efficient for producing tidal tails. Our observations suggest that the H I at larger galactic radii has been ejected to form the tails and the remnant H I disks have been perturbed by the interaction. In particular, we find that the H I disk of NGC 6670E appears to have been nearly destroyed. We conclude that the previous encounter between the galaxies had a large impact parameter and that the system is still in an early stage of interaction.

Even though NGC 6670 is in an early stage of interaction, we find that there is evidence for nuclear starbursts already present. The CO(1–0) observations show large molecular gas reservoirs in the central regions and the 20 cm radio continuum observations reveal enhanced star formation activity in the nuclear regions of both galaxies.

---

<sup>1</sup>Academia Sinica Institute of Astronomy and Astrophysics, P.O. Box 1-87, Nankang, Taipei, Taiwan

<sup>2</sup>IPAC, MS 100-22, Caltech, 770S Wilson Ave., Pasadena, CA 91125, USA

<sup>3</sup>Laboratory for Astronomical Imaging, Department of Astronomy, University of Illinois, 1002 W. Green Street, Urbana, IL 61801, USA

<sup>4</sup>Current address: Institute for Astronomy, University of Hawaii, 2680 Woodlawn Drive, Honolulu, HI 96822, USA

The spatial extent of the 20 cm emission and the FIR-radio correlation further rule out active galactic nuclei as the source of the IR luminosity from NGC 6670. We estimate the ratio  $L_{\text{IR}}/M_{\text{H}_2}$ , which is often used as an indicator of star formation efficiency, in the nuclear regions of NGC 6670E and NGC 6670W to be 18 and 11  $L_{\odot}/M_{\odot}$ , respectively. The nuclear star formation efficiency of these two galaxies has been elevated to the level observed in other nearby starburst galaxies ( $L_{\text{IR}}/M_{\text{H}_2} > 10L_{\odot}/M_{\odot}$ ). Other indicators of starburst activity such as CO brightness temperature and infrared surface brightness are also observed.

*Subject headings:* galaxies: individual (NGC 6670, CGCG 301-032) — galaxies: interactions — galaxies: kinematics and dynamics — galaxies: starburst — infrared: galaxies — radio continuum: galaxies — radio lines: galaxies

## 1. Introduction

Luminous infrared galaxies (LIRGs) are galaxies with infrared luminosity  $L_{\text{IR}}(8\text{--}1000 \mu\text{m})$  greater than  $10^{11}L_{\odot}$ . LIRGs are also the most numerous sources with bolometric luminosity greater than  $10^{11}L_{\odot}$  in the local universe (see Sanders & Mirabel (1996) for a recent review as well as the definition of infrared luminosity). Observations have shown that the large IR luminosity of LIRGs is primarily due to intense starbursts in the nuclear regions and that dust-enshrouded active galactic nuclei (AGNs) may only play a minor role in some ultraluminous (ULIRG,  $L_{\text{IR}} > 10^{12}L_{\odot}$ ) systems (Joseph & Wright 1985; Rieke et al. 1985; Condon et al. 1991; Genzel et al. 1998; Downes & Solomon 1998; Smith et al. 1998). For starbursts to produce the infrared luminosity of LIRGs, more than  $10^9M_{\odot}$  of young massive stars are needed to heat the interstellar dust. This requires a concentration of at least  $10^9M_{\odot}$  of molecular gas in a very small region ( $\sim 1$  kpc) to form these stars (cf. Lo et al. (1987)).

Most LIRGs are found in interacting/merging systems (Sanders et al. 1988; Melnick & Mirabel 1990; Murphy et al. 1996; Duc, Mirabel, & Maza 1998) that are rich in molecular gas (Sanders et al. 1991; Solomon, Downes, & Radford 1992; Solomon et al. 1997; Gao & Solomon 1999). The fraction of the LIRGs in interacting/merging systems increases with infrared luminosity, from  $\sim 10\%$  at  $L_{\text{IR}} = 10^{10.5} - 10^{11}L_{\odot}$  to  $\sim 100\%$  at  $L_{\text{IR}} > 10^{12}L_{\odot}$  (Sanders et al. 1988; Sanders & Mirabel 1996; Melnick & Mirabel 1990; Murphy et al. 1996). This suggests that galaxy-galaxy interactions play a major role in triggering starbursts in molecular gas-rich galaxies. A commonly discussed interpretation of the triggering mechanism is that, during the interaction, the gas clouds experience tidal torque produced by either the host galaxy or the companion. The clouds which lose their angular momentum flow into the circum-nuclear regions of the host galaxies. As a result, the concentration and compression of molecular gas in the circum-nuclear regions give rise to starbursts. Furthermore, during the final stage of the galaxies' merging, clouds with small angular momentum may flow into the galactic nuclei and then trigger an AGN or an ultraluminous starburst. This

scenario, however, has not been confirmed by observations. Moreover, only a small fraction of optically selected interacting/merging systems are truly IR luminous or show other elevated tracers of star formation (Arp 1966; Kennicutt et al. 1987; Bushouse, Werner, & Lamb 1988). There also exist LIRGs which are gas-rich interacting galaxies but are not undergoing starbursts (e.g., Arp 302 (Lo, Gao, & Gruendl 1997)). Apparently, galactic interaction is not the only causal factor in the enhanced IR luminosity.

Recent numerical simulations of the merging of gas-rich spiral galaxies have shown how the gas and stars may be redistributed during the interaction (Barnes & Hernquist 1991; Mihos, Bothun, & Richstone 1993; Mihos & Hernquist 1996). The simulations can predict a sharp rise and fall in star formation rate (SFR) in the nuclear regions of galaxies, by assuming the SFR is proportional to some power of the gas density (e.g., the Schmidt law). On the other hand, the physical meaning of the Schmidt law itself is still unclear and a range of power indices for the Schmidt law are suggested by observations (Scoville, Sanders, & Clemens 1986; Kennicutt 1998; Taniguchi & Ohyama 1998). It is difficult to assess whether or not these simplified recipes which relate gas density to star formation produce realistic results. Furthermore, Jog & Solomon (1992) showed that compression of giant molecular clouds due to the over-pressure produced by H I cloud-cloud collisions in colliding galaxies can produce starbursts in off-nuclear regions. On the other hand, simulations (Mihos, Bothun, & Richstone 1993) fail to reproduce the gas concentrations in the off-nuclear regions in systems like Arp 244 and Arp 299 (see, e.g., Stanford et al. (1990); Sargent & Scoville (1991); Mirabel et al. (1998)). Therefore, a detailed understanding of where and when starbursts take place, as well as the physical mechanism responsible for triggering them, remains unknown.

Previous observational studies of starbursts in LIRGs have mostly concentrated on ultraluminous or advanced merging systems (e.g., Lo et al. (1987); Sanders et al. (1988); Scoville et al. (1991); Genzel et al. (1998)). In such systems, the interstellar medium (ISM) has already been highly disrupted by the tidal interaction and the starbursts. Therefore, these observations can only provide limited comparison with the models. In order to trace the distribution of gas and the evolution of starbursts along the merging process, we started a program of multi-wavelength observations to study a sample of LIRGs in early/intermediate merging phases. Partial results of this program can be found in Lo, Gao, & Gruendl (1997), Gao et al. (1997), Hwang et al. (1999), Gao et al. (1999), Lo et al. (2000), and Gao et al. (2001). The goal is to sample the evolution of the ISM properties in LIRGs and to verify observationally the proposed triggering mechanisms of starbursts.

In this paper, we present interferometric observations of the H I 21 cm line, the 20 cm radio continuum, and the CO(1–0) line emission of NGC 6670 (UGC 11284). NGC 6670 consists of two edge-on disk galaxies with an angular separation of  $\sim 27''$  between the two nuclei. At a redshift ( $cz$ ) of  $8684 \text{ km s}^{-1}$ , its distance is 120 Mpc ( $H_0 = 75 \text{ km s}^{-1} \text{ Mpc}^{-1}$ ,  $q_0 = 0.5$ ) and the projected nuclear separation is  $\sim 16 \text{ kpc}$ . Near infrared (NIR) images of NGC 6670 show a slightly warped disk (the western galaxy, NGC 6670W) and another disk (the eastern one, NGC 6670E) with a mildly distorted shape. The disks appear to just touch each other in the sky plane. Because of the

edge-on geometry and the lack of optical tidal features, it is difficult to determine the interaction history, the orbital geometry of this system, or even whether the galaxies are spatially related or superposed by chance. As the neutral hydrogen gas has a more extended distribution than stars and is less bound to the parent galaxies, it is a sensitive tracer of gravitational perturbation. Imaging the H I emission provides the unique opportunity to verify the interaction between the galaxies of NGC 6670.

The infrared luminosity of NGC 6670 is  $3.8 \times 10^{11} L_{\odot}$ . Single-dish measurements show a total CO flux of  $220 \text{ Jy km s}^{-1}$ , which corresponds to a molecular gas mass of  $\sim 3.9 \times 10^{10} M_{\odot}$  (Gao 1996; Gao & Solomon 1999). The global ratio of  $L_{\text{IR}}/M_{\text{H}_2} \equiv \text{SFE}$  is often used as an indication of star formation efficiency, the star formation rate per unit molecular gas mass. In NGC 6670, the global SFE is  $10 L_{\odot}/M_{\odot}$ , only a factor of 2 higher than the average SFE of the giant molecular clouds (GMCs) in the Milky Way’s disk (Scoville & Good 1989) and of the isolated galaxies (Young & Scoville 1991). Without knowing the distributions of molecular gas and star formation activity, one cannot tell whether the large IR luminosity of NGC 6670 is due to nuclear starbursts ( $\text{SFE} > 20 L_{\odot}/M_{\odot}$ , (Scoville et al. 1991; Bryant & Scoville 1999)) induced by the interaction, or simply due to the large reservoir of molecular gas with a rather ordinary SFE as in Arp 302 (Lo, Gao, & Gruendl 1997). The Infrared Space Observatory (ISO) mid-infrared observations of NGC 6670 suggest that most of the mid-infrared emission comes from extended circum-nuclear starbursts but not from dust enshrouded AGNs (Hwang et al. 1999). Our CO(1–0) and 20 cm interferometric observations provide a higher resolution view that allows us to investigate the distribution of molecular gas and star formation.

## 2. Observation and Data Reduction

### 2.1. Optical and Near-Infrared Observations

Broad-band optical *R*-band and near-infrared *J*-band images of the NGC 6670 system were acquired using the 1-m telescope at Mt. Laguna Observatory. *R*-band observations of NGC 6670 were taken with a  $2048 \times 2048$  CCD on 1997 August 2. These images were bias and flat-field corrected, cosmic-ray hits were rejected, and the individual exposures were coadded to form the final image with 720 seconds total integration time and  $2''.4$  spatial resolution.

The *J*-band observations were obtained with the NIRIM camera (Meixner, Young Owl, & Leach 1999) on the 1-m telescope at Mt. Laguna Observatory on 1998 May 19. The camera was configured such that the  $256 \times 256$  NICMOS 3 array was operating at a  $1''$  per pixel plate scale. The objectives of these observations were to image the region around and between the NGC 6670 system and the companion galaxy CGCG 301-032 (IRASF 18335+5949) roughly  $5'$  to the southeast. To this end, a field  $13'.5 \times 6'.8$  was imaged in  $94 \times 60$  second exposures. The individual exposures were taken in a sequence that included 2 sky (off-source) exposures after every 3 on-source exposures. A first-order sky subtraction was achieved by subtracting the median of the four

off-source exposures which temporally bracketed each on-source exposure. The spatial offsets of the resulting 53 on-source frames were determined from field stars and then the zero-point offset between all overlapping frames were calculated. A non-linear least-squares solution was used to determine the best zero-point offset for each frame (Regan & Gruendl 1995) before the frames were combined into a final mosaic image of the entire field. The typical resolution measured from stars in the final mosaic image was  $2''.7$

Additional optical broad-band images were acquired from the Issac Newton Group Archive. These observations were made on 1995 May 24 with the 1-m Jacobus Kapteyn Telescope at La Palma at  $B$ ,  $V$ , and  $I$ -band, with integration times of 900, 600, and 900 seconds respectively. These images, along with the associated bias and flat-field measurements, were retrieved from the archive. The images were bias and flat-field corrected and cosmic-ray hits were removed. The resulting  $B$ ,  $V$ , and  $I$ -band images have spatial resolutions of  $1''.5$ ,  $1''.3$ , and  $1''.2$  respectively.

In addition, a near-infrared  $K'$ -band image (D.-C. Kim and D. B. Sanders, private communication) with  $\sim 1'.5$  field of view, obtained with the University of Hawaii 88-inch telescope on Mauna Kea, is included for comparison with our radio images. NGC 6670 was one of the targets in their optical/near-infrared imaging survey of extended Bright Galaxy Sample galaxies (see Sanders et al. (1995); Sanders et al., in preparation). Astrometric solutions for all the optical and near-IR observations were obtained by using stars from the Hubble Guide Star Catalog 1.2, the typical uncertainty in the registration of any of the optical images is less than  $0''.5$ .

## 2.2. 21 cm H I Observation

H I observations were obtained with the NRAO Very Large Array (VLA) C configuration on 1997 September 13. The total usable integration time on NGC 6670 was nearly 3 hours. The radio source 3C 286 was observed for flux and bandpass calibration at the beginning of the observation. The phase calibrator 3C 343 was observed for 60–90 seconds before and after every 40 minutes of on-source integration of NGC 6670. The observing frequency was 1.38056 GHz, corresponding to  $cz=8650$  km s $^{-1}$ . With on-line Hanning smoothing and a total of 63 channels over a bandwidth of 6.25 MHz, the channel resolution was 21.8 km s $^{-1}$ .

The interferometric data were reduced with the NRAO *AIPS* package. The calibrated  $u$ - $v$  data were inverted to image cubes using uniform weighting and Briggs' Robust Weighting (Briggs 1995). When applying Robust Weighting, we chose the parameter  $ROBUST = +1.2$  for the imaging task *IMAGR*. The fitted synthesized beams are  $16''.3 \times 11''.4$  at  $51^\circ 2$  position angle for uniform weighting and  $19''.1 \times 15''.6$  at  $61^\circ 5$  for Robust Weighting. After the *CLEAN* algorithm was applied, an  $11''.4$  circular restoring beam was used for the uniformly weighted cube and an  $18''.0 \times 15''.6$  beam at  $61^\circ 5$  was used for the cube of Robust Weighting. A continuum map was obtained from each cube by averaging the line-free channels 5–18, which corresponds to the heliocentric velocity between 9239 km s $^{-1}$  and 8955 km s $^{-1}$ . The continuum map was then subtracted from each cube to obtain a

cube containing only H I emission. In the resulting continuum-free cubes of uniform and Robust Weighting, the noise levels ( $\sigma$ ) are 0.50 and 0.35 mJy beam<sup>-1</sup> ( $\sim$  2.3 K and 0.74 K brightness temperature), respectively. A correction for the primary beam pattern was then applied to the continuum-free cubes. Moment maps were then made from both cubes using the standard *MOMENT* task to produce the integrated intensity maps, the intensity-weighted radial velocity maps, and the intensity-weighted velocity dispersion maps.

### 2.3. 20 cm Radio Continuum Observation

NGC 6670 was observed at 20 cm with the B array configuration of the VLA on 1997 March 9. Two intermediate frequencies were centered at 1.4649 and 1.3851 GHz with 50 MHz bandwidths. The radio source 3C48 (0137+331) was observed for 6 minutes for flux and bandpass calibration. The phase calibrator, 1927+612, was observed for 1.5 minutes before and after every 15 minutes of integration on NGC 6670. The total integration time on NGC 6670 was 1 hour. The NRAO *AIPS* package was used for data reduction. The visibilities were uniformly weighted, Fourier transformed, and then cleaned. The “dirty” beam was fitted to be  $5''.9 \times 3''.1$  at an  $83^\circ.3$  position angle and a circular restoring beam of  $3''.1$  was used after the *CLEAN* algorithm had been applied. The noise level in the restored map is  $4.7 \times 10^{-2}$  mJy beam<sup>-1</sup> which corresponds to 2.7 K brightness temperature.

### 2.4. CO(1–0) Observations

We observed NGC 6670 in the CO( $J = 1-0$ ) transition with the Berkeley-Illinois-Maryland Association (BIMA) millimeter array (Welch et al. 1996) in 1996 and 1997 using the 9-element C configuration and the 10-element B configuration. The digital correlator was used with the widest available bandwidth to cover a velocity range of 1,600 km s<sup>-1</sup>, at a resolution of 8.4 km s<sup>-1</sup>. The  $\sim 2'$  primary beam was centered between the two galaxies to best cover the emission from this system which extends slightly more than  $1'$ . The observing frequency was 112.0567 GHz, corresponding to the CO(1–0) line at the median redshift  $cz=8,600$  km s<sup>-1</sup> of this galaxy system. The nearby quasar, 1824+568, was observed for 8 minutes every half an hour to obtain the antenna phase and amplitude gain calibration. The strong quasar 3C454.3, and a planet (Mars or Uranus) were also observed for each track to obtain a flux calibration. Observations were obtained on seven different dates with typical system temperatures between 250 and 800 K. The total on-source integration time for NGC 6670 was 24 hours.

The interferometric data were reduced with the *MIRIAD* data reduction package (Sault, Teuben, & Wright 1995). Data cubes of the CO brightness distribution,  $T_b(x, y, V)$ , where  $x$  and  $y$  are the spatial coordinates and  $V$  is the radial velocity were made at 20 km s<sup>-1</sup> resolutions. Two different spatial resolutions were obtained by applying different weight functions to the

visibilities prior to the Fourier transformation. First, all visibilities were weighted by the system temperature at the time of the observation, then two different weight functions were applied to achieve two different resolution data cubes. The first case was chosen to produce a synthesized beam with roughly natural weighting but sidelobes in the dirty synthesized beam were suppressed by using the Briggs’ Robust Weighting (Briggs 1995) to determine the specific weighting of each visibility. In the second case Briggs’ Robust Weighting was also used but an additional Gaussian taper was applied to the visibilities to down-weight the long-baseline B-array data.

After the Fourier transform of the visibilities produced a dirty map, the *MIRIAD CLEAN* algorithm was used to remove sidelobe response and produce final CO cubes. The final CO cubes cover a range from  $-500$  to  $+500$  km s $^{-1}$  about the systemic velocity ( $cz=8,600$  km s $^{-1}$ ). The cubes resulting from this reduction with the two different weighting schemes have final synthesized beams of  $2''.7 \times 2''.1$  and  $5''.4 \times 4''.6$ . The root-mean-square (rms) noise level is 13 mJy beam $^{-1}$  (0.2 K brightness temperature) in each channel of the high resolution clean cube and is 15 mJy beam $^{-1}$  (0.05 K) in each channel of the low resolution clean cube. Moment maps were then made to produce the integrated intensity maps and the intensity-weighted radial velocity maps.

### 3. Results

#### 3.1. Optical to Near-IR Morphology of NGC 6670

Based on previous observations, Zwicky (1971) described the morphologic components of the NGC 6670 system as a “post-eruptive quadruple system of three brush-like and one spherical compact” galaxies. Figure 1 shows optical and near-infrared ( $B, V, R, I, J, K'$ -band) images of the NGC 6670 system. These images reveal that the two largest galaxies in this system are a pair of nearly edge-on spiral galaxies. The relatively weak bulges of these two galaxies, compared to the disks, suggest that these two galaxies are late type spiral galaxies. To the southeast of the nucleus of NGC 6670E (the eastern spiral) there is a bright but fuzzy feature in shorter wavelengths. At NIR wavelengths, especially in the  $K'$ -band, it appears more like a part of NGC 6670E’s disk. The different appearance between longer and shorter wavelengths in this region can be due to either dust extinction or a large amount of blue stars. This feature could be a dusty region, or a young stellar tidal feature in the outer disk of NGC 6670E, or a separate dwarf galaxy. Furthermore, the CO morphology, CO kinematics (§ 3.3), and radio continuum morphology (§ 3.4) all suggest only two edge-on disks in this system. It is most likely that the fuzzy feature in the southeast end of NGC 6670E is part of its disk or a young stellar tidal feature.

The western spiral galaxy (NGC 6670W) appears to be the more edge-on of the two spiral galaxies. At NIR wavelengths a prominent bulge is evident, while at blue wavelengths the bulge and eastern portion of the disk are barely detected. This is likely due to dust extinction in the eastern part of the disk. We note that the heavily obscured region in the eastern part of the disk of NGC 6670W is also the location of the huge H I concentration (the “C concentration,” see § 3.2.1).

It is possible that this H I concentration is responsible for the extinction. The western half of the disk is in general brighter than the eastern half especially at shorter wavelengths. This may be an indication of recent star formation. Both the eastern and western halves of the disk in NGC 6670W show significant curvature. This morphology could be attributed to: 1) a warped disk, 2) a two-armed grand-design spiral with large pitch angle, inclined at nearly perfect edge-on, or 3) a tidal perturbation that is nearly in the plane of the galaxy.

In contrast to NGC 6670W, the nuclear region of NGC 6670E is clearly detected in all of the broad-band images. Furthermore, the disk appears less edge-on, with surface brightness variations that differ from one band to the next. These morphological variations could be attributed to dust extinction and/or massive star formation. On the other hand, if the emission detected at  $B$ -band traces star formation in the absence of dust, then the star formation in the nuclear region of NGC 6670E is prolific in comparison to the nucleus/bulge of NGC 6670W.

The “brush-like” features noted by Zwicky (1971) can all be attributed to the disks of the two spiral galaxies. One of these, the eastern portion of NGC 6670W disk, appears to extend to “touch” NGC 6670E. This is most clear in the  $K'$ -band image. In all the broad-band images, the disks of both NGC 6670E and NGC 6670W are enveloped in a faint “halo” of star light. This “common envelope,” the disturbed morphologies of both disks, and the apparent proximity of the disks suggest that the true separation between the two galaxies is not much larger than the projected separation and the galaxies may be interacting. On the other hand, none of these clues, along or together, prove that the two galaxies are interacting, much less in physical contact.

## 3.2. H I Results

### 3.2.1. Distribution of H I in NGC 6670

In Figure 2, we present the low resolution (robust weighting) H I integrated intensity map and the intensity-weighted velocity map. Figure 3 shows an enlarged view of the high resolution (uniform weighting) H I integrated intensity. For comparison, CO(1–0) integrated intensity is also plotted in Figure 3 (see § 3.3.1). Several observed quantities are summarized in Table 1.

A previously unknown long H I tail is revealed to the west of the stellar disks of NGC 6670 (hereafter named the “W tail,” see Fig. 2). The W tail has a projected extension of  $\sim 90$  kpc from the center between the two galaxies. Furthermore, a smaller H I tail extends  $\sim 25$  kpc away from NGC 6670 in the northeast direction (the “NE tail”). Neither tail has any obvious optical counterparts. The existence of H I tidal tails manifests that the galaxies in NGC 6670 are interacting, and are not by chance superposed.

The H I radial velocity map (Fig. 2b) and the H I spectra (Fig. 4) show that in NGC 6670, the largest blueshift ( $8360 \text{ km s}^{-1}$ ) appears in the W tail and the largest redshift ( $8820 \text{ km s}^{-1}$ ) appears in the NE tail. The velocity of the whole system increases systemically from the W tail



to the NE tail. The H I velocity dispersion (cf. Fig. 4 and Table 1) in each tail is relatively small, between  $11 \text{ km s}^{-1}$  and  $17 \text{ km s}^{-1}$ . The velocity of the W tail varies between  $8432$  and  $8366 \text{ km s}^{-1}$  (Fig. 4) and the velocity difference between the end and the middle of the W tail is less than  $20 \text{ km s}^{-1}$ . The NE tail only appears in the channels of  $8825$  and  $8803 \text{ km s}^{-1}$ . The opposite sense of velocity and the relatively narrow velocity range of the H I tails in NGC 6670 are very similar to the H I properties on the tails of the intermediate-stage merger Arp 244 (*The Antennae*, van der Hulst (1979)) and the early-stage merger NGC 4676 (*The Mice*, Hibbard & van Gorkom (1996)). On the other hand, only 25% of NGC 6670’s H I emission comes from the two tails, in contrast with Arp 244 and NGC 4676 which have more than 60% of their H I distributed along the tails. With the trend found by Hibbard & van Gorkom (1996) that late stage mergers have more H I outside the stellar disks than early stage mergers, NGC 6670 is most likely in an early stage of interaction. This is consistent with the mild distortion of the disks revealed at optical and NIR wavelengths.

The total H I flux of NGC 6670 (including the tails), obtained by adding all the flux in the low resolution channel maps (Fig. 5), is  $4.83 \text{ Jy km s}^{-1}$ . The single dish H I flux of NGC 6670 measured by Martin, Bottinelli, & Gouguenheim (1991) is  $4.19 \text{ Jy km s}^{-1}$ , which is comparable with our results. Their result may be a lower limit because their half-power beam width in the east-west direction ( $4'$ ) is similar to the source extent and they might have missed parts of the extended H I tails. In addition, the most recent results of van Driel, Gao, & Monnier-Ragaine (2001) suggest that the H I flux in Martin et al. may be systematically lower by up to 30%. Taking this into consideration, we tend to conclude that our VLA observation has probably detected almost all of the H I flux in this system.

The H I intensity map (Fig. 2) shows that most of the H I in NGC 6670 is around the two separated stellar disks and forms a common H I halo. Three concentrations of H I gas can be identified near the stellar disks: the “W concentration” in western part of the NGC 6670W disk, the “C concentration” between the two galaxies, and the weaker “E concentration” in eastern part of the NGC 6670E disk (Fig. 2a and Fig. 3). All three H I concentrations are located at the ends of the stellar disks with the C concentration in the “interaction region” between the stellar disks. These three H I concentrations are also the most remarkable features near the main body of the galaxies in the channel maps (Fig. 5), especially the C concentration. In the higher resolution map (Fig. 3), the C concentration is marginally resolved by the  $12''$  beam and appears to extend toward the north-eastern direction. The compact W concentration remains unresolved in the high resolution map.

The H I gas mass is estimated using the formula (Roberts 1975):

$$M_{\text{HI}}(M_{\odot}) = 2.36 \times 10^5 D^2 \int S dv,$$

where  $D$  is the distance in Mpc, and  $\int S dv$  is the H I integrated flux in  $\text{Jy km s}^{-1}$ . The H I gas masses of the whole NGC 6670 system, the W tail, and the NE tail obtained from the low resolution channel maps are  $1.6 \times 10^{10} M_{\odot}$ ,  $3.3 \times 10^9 M_{\odot}$ , and  $8.1 \times 10^8 M_{\odot}$ , respectively. The H I mass within the C and W concentrations obtained from the high resolution channel maps is  $2.0 \times 10^9 M_{\odot}$  and

$1.4 \times 10^9 M_{\odot}$ , respectively. We further estimate the H I peak and averaged column density in the C and the W concentration in the high resolution integrated intensity map (made with  $1.5 \sigma$  flux clipping). The results are listed in Table 1. Because the W concentration is unresolved and the C concentration is only slightly larger than the beam, the measured peak column densities should be regarded as lower limits.

As mentioned in § 3.1, the C concentration is located in the place where the heaviest dust obscuration occurs. The visual extinction caused by the C concentration can be estimated with the relation  $A_V \sim n_{\text{HI}}/2 \times 10^{21} \text{cm}^{-2}$ . Using the peak H I column density listed in Table 1, we estimate the visual extinction to be  $\sim 1$  magnitude. This is a lower limit because individual H I clouds in the C concentration are unresolved and may have column densities higher than the value used here. Furthermore, molecular gas could also be present. It seems likely that the C concentration contributes to, if not dominates, the extinction in the eastern portion of the disk of NGC 6670W. If this is true, the fact that there is not obvious extinction in the western half of the NGC 6670E disk would imply that NGC 6670W is in the background, relative to NGC 6670E. We will discuss the geometry of this interacting system in details in § 4.1.3.

### 3.2.2. H I Kinematics in NGC 6670

In Figure 6, we present H I position-velocity ( $p$ - $v$ ) diagrams along the major axes of stellar/molecular disks and along a slice joining the two nuclei. For comparison, we also overlay the CO  $p$ - $v$  diagrams (see § 3.3.2) along the same slices used for the H I. On the large scale, the motion of H I near the two stellar disks appears as a single rotating system. Unlike in the CO  $p$ - $v$  diagrams, it is hard to see two distinct H I systems (Fig. 6c). This is also true in the channel maps (Fig. 5). In the channel maps, from  $v = 8345$  to  $8760 \text{ km s}^{-1}$ , the location of H I emission changes systematically from the west to the east. An explanation to this is that the H I gas originally in the two disks is now merging into a single dynamical system. On the other hand, the CO velocity field suggests the galaxies have similar spin directions (§ 3.3.2). It is also possible that the apparent global H I kinematics is just a result caused by chance matching of the velocities of the galaxies.

The H I near the disk of NGC 6670W (Figure 6b) shows a constant velocity gradient over the length of the optical disk (between  $-20''$  and  $+20''$ ). The H I emission along the velocity gradient is weakest near the systemic velocity of NGC 6670W,  $8570 \text{ km s}^{-1}$ , which is determined by the CO velocity field (§ 3.3.2). The stronger H I emission is located near the ends of the optical disk (the C and W concentrations). The constant velocity gradient and the edge-brightened morphology in the  $p$ - $v$  diagram suggest that the H I gas is in a rotating ring-like structure around NGC 6670W. The rotation velocity of the H I ring is  $\sim 150 \text{ km s}^{-1}$ , slightly lower than the rotation velocity of the molecular disk which is  $\sim 175 \text{ km s}^{-1}$  (§ 3.3.2). The edge-on H I ring partially explains the existence of the C concentration and the W concentration.

The H I  $p$ - $v$  diagram for NGC 6670E (Fig. 6a) has a more complex appearance than that for

NGC 6670W. There is a lack of H I emission near the center of NGC 6670E at the systemic velocity suggested by the CO velocity field, around  $v = 8730 \text{ km s}^{-1}$  (§ 3.3.2). Most of the H I emission at the center position comes from a small peak centered between  $-2''$  and  $+8''$  at  $8630 \text{ km s}^{-1}$ . This gas cannot be in a circular orbit and its velocity suggests either  $100 \text{ km s}^{-1}$  infall or outflow relative to the center of NGC 6670E. Also present in the H I  $p$ - $v$  diagram of NGC 6670E are the C and E concentrations. The E concentration appears to roughly match the CO velocity in the eastern part of NGC 6670E. Two velocity components of the C concentration at  $v = 8650$  and  $8715 \text{ km s}^{-1}$  appear to associate with the western disk of NGC 6670E and also the eastern disk of NGC 6670W (Fig. 6b,c). Overall, the H I velocity distribution in NGC 6670E is neither like a rotating ring (e.g., H I in NGC 6670W), nor like a rotating disk (e.g., CO in NGC 6670E). This suggests that the H I disk of NGC 6670E has almost been destroyed. The clear deviation from circular rotation of H I in NGC 6670E is another strong indication of a tidal interaction between the galaxies besides the apparent H I tidal tails.

The C concentration shows two velocity components ( $v = 8715$  and  $8650 \text{ km s}^{-1}$ ) that can be interpreted as belonging to either or both galaxies. It is interesting to note that both the E and W concentrations have velocities close to the CO velocities in the same regions. On the other hand, only the weaker  $8650 \text{ km s}^{-1}$  component of the C concentration appears to match the CO velocity of the western part of NGC 6670E. The strongest component ( $8715 \text{ km s}^{-1}$ ) has a velocity between the CO velocities of the eastern part of NGC 6670W ( $8740 \text{ km s}^{-1}$ ) and the western part of NGC 6670E ( $8660 \text{ km s}^{-1}$ ). This makes the outer H I in both galaxies appear to have lower circular velocities than the molecular gas in the inner disks.

As mentioned earlier in this section, the global apparent H I kinematics could be explained by the merge of H I disks or by matching up the H I velocities of the disks by chance. The apparent lower H I rotation velocities in both disks and the existence of the C concentration could also be explained by these two scenarios. First, if the H I disks were interacting with each other and merging into a single system, the C concentration might result from a direct interaction between the H I disks. In other words, cloud-cloud collisions, ram pressure, or tidal stripping in the prograde-prograde (§ 3.3.2) interaction may be forming a large gas reservoir in the region between the galaxies. The collisions may slow down the velocities of the H I clouds between the disks and produce the observed H I velocity profiles. In this scenario, the C concentration is a true concentration of H I clouds in space. On the other hand, it is also possible that the two H I disks are spatially separated along the line of sight. Instead of direct collisions, the lower H I rotation velocities might result from loss of angular momentum due to a tidal torque from the interaction. Therefore, in the region between the galaxies, the H I clouds from the two disks have velocity difference smaller than that suggested by CO rotation curves. In this scenario, the C concentration is a superposition of two independent structures along the line of sight.

The most important difference between these two scenarios is whether or not the two H I components of the C concentration are approaching each other. As mentioned in § 3.2.1, it is suggested that NGC 6670W is behind NGC 6670E. Consequently, the CO velocities of the eastern

part of NGC 6670W and the western part of NGC 6670E suggest that the H I clouds from the two disks in the C concentration must be moving away from each other if there is no strong interaction between the H I clouds. On the other hand, a direct interaction requires the H I clouds to be approaching each other. These two possibilities can be distinguished if we can tell which H I component belongs to which galaxy. However, this is not possible no matter in the  $p$ - $v$  diagrams or the channel maps in our current H I data of very limited resolution. Higher resolution H I observations may help to answer this.

### 3.3. CO(1–0) Results

#### 3.3.1. Distribution of the Molecular Gas

Our BIMA CO(1–0) observations reveal the distribution of the molecular gas in NGC 6670. In Figure 7, we present the CO(1–0) channel maps of NGC 6670 at  $2''.7 \times 2''.1$  resolution. In Figure 8, we present the CO integrated intensity at resolution of  $5''.4 \times 4''.6$  (Fig. 8a, hereafter the low resolution) and  $2''.7 \times 2''.1$  (Fig. 8b, hereafter the high resolution). The CO emission in NGC 6670 is distributed along the inner part of the optical disk in each galaxy. No CO emission was detected in the H I tail regions outside the optical disks. Little CO emission is detected from the region where the stellar disks overlap (Fig. 7,  $v = 8660$  and  $8680$  km s<sup>-1</sup>). Near the center of NGC 6670W, the CO emission appears to extend slightly in the direction perpendicular to the disk. In NGC 6670E, the CO distribution is more distorted and deviates from the symmetric disk morphology. Both the CO morphology and the H I kinematics shown in Figure 6 suggest a stronger tidal perturbation on the disk of NGC 6670E.

In Figure 8b, the distribution of dust absorption as suggested by the  $B$ -band image seems to correlate with the molecular gas distribution. Therefore, it seems plausible that the molecular gas in the eastern part of the NGC 6670W disk contributes to the extinction in this region. On the other hand, it is suggested in Figure 3 that the H I C concentration may also contribute to the extinction. The H<sub>2</sub> column density in this region is an order of magnitude higher than the lower limit of the peak H I column density. However, comparing to the H I, the molecular clouds in NGC 6670W are distributed more symmetrically over the whole disk. It is unlikely that all the H<sub>2</sub> in the eastern part of the NGC 6670W disk contributes to the extinction because some molecular clouds in the edge-on disk may be behind the stars. It is not clear in our observations which gas component in the eastern part of the disk of NGC 6670W has more contribution to the extinction.

The CO(1–0) images show that the large molecular reservoirs are located in the central regions of the disks. We measure the CO integrated flux in the inner regions of the two galaxies from the high resolution channel maps. We find that 56% of the CO flux from NGC 6670E is concentrated in the inner 4 kpc region. In NGC 6670W, 48% of its CO flux comes from the inner 4 kpc region. The molecular gas distribution in both NGC 6670W and NGC 6670E is clearly concentrated toward the central region, especially knowing that the extent of the stellar disks of both galaxies is  $\gtrsim 20$  kpc.

The total CO integrated flux is determined using the high resolution channel maps (Fig. 7). The total flux is  $65.4 \text{ Jy km s}^{-1}$  for NGC 6670E and is  $149.7 \text{ Jy km s}^{-1}$  for NGC 6670W. The total flux of the NGC 6670 system measured by the BIMA array is the same, within the errors, as the single dish value of  $220 \text{ Jy km s}^{-1}$  (Gao 1996; Gao & Solomon 1999). The shapes of the integrated CO spectra of NGC 6670E and NGC 6670W (Fig. 9) are also similar to the single dish spectra of Gao & Solomon (1999). These comparisons suggest that the interferometric observations did not systematically miss CO emission.

We estimate the molecular gas mass from the integrated CO(1–0) flux using the empirical relation (Scoville et al. 1987):

$$M_{\text{H}_2}(M_{\odot}) = 1.18 \times 10^4 D^2 \int S dv,$$

where  $D$  is distance in Mpc and  $\int S dv$  is CO integrated flux in  $\text{Jy km s}^{-1}$ . Here the Galactic CO-to- $\text{H}_2$  conversion factor  $X \equiv N(\text{H}_2)/I_{\text{CO}} = 3.0 \times 10^{20} \text{ cm}^{-2} (\text{K km s}^{-1})^{-1}$  (see Young & Scoville (1991) for a review) is assumed for convenient comparison with previous results. We note that this conversion factor may lead to an overestimate of the molecular gas mass if the galaxy is undergoing starbursts (see e.g., Maloney & Black (1988); Bryant & Scoville (1999)). The estimated total molecular mass is  $1.1 \times 10^{10} M_{\odot}$  for NGC 6670E and is  $2.5 \times 10^{10} M_{\odot}$  for NGC 6670W.

We estimate the peak edge-on molecular column density in the inner 2 kpc region of each galaxy using the high resolution integrated intensity map. The results are listed in Table 2. It is difficult to obtain a precise face-on column density for these two galaxies. This is mainly because of the irregular CO morphology in the outer disks and therefore there is a large uncertainty in determining the outer disk contribution to the edge-on column density. To simplify the estimation, we assume that the CO flux measured in the central 2 kpc regions in the image has no outer disk contribution and all comes from the inner disks. The estimated central face-on column density is close to the edge-on values ( $\sim 10^3 M_{\odot} \text{ pc}^{-2}$ ). The molecular hydrogen column density is large compared with that of the Milky Way’s disk ( $4\text{--}20 M_{\odot} \text{ pc}^{-2}$ ) and center ( $40\text{--}300 M_{\odot} \text{ pc}^{-2}$  (Sanders, Solomon, & Scoville 1984)) but small compared with that of the LIRGs at the more advanced merging stages (typically greater than  $10^4 M_{\odot} \text{ pc}^{-2}$ , see e.g., Bryant & Scoville (1999); Yun & Scoville (1995); Solomon, Downes, & Radford (1992)).

Combining with the results of our VLA H I 21 cm observation, the total gas content (atomic + molecular) in this system is  $\sim 5.3 \times 10^{10} M_{\odot}$  and the global ratio of  $M_{\text{H}_2}$  to  $M_{\text{HI}}$  is 2.2. According to the study of Young & Knezek (1989), Sab and Sb spiral galaxies have a ratio of  $M_{\text{H}_2}/M_{\text{HI}}$  around 2 and spiral galaxies later than Sc have a ratio smaller than 1. The optical morphology of NGC 6670 suggests that the two disks are late type spiral galaxies. The slightly high global ratio of  $M_{\text{H}_2}$  to  $M_{\text{HI}}$  for NGC 6670 might be interpreted as due to an enhanced conversion of atomic to molecular gas. Furthermore, roughly 25% of H I gas in NGC 6670 is in widely extended tidal tails and roughly 22% is additionally concentrated outside the disks. The ISM in the inner galactic disks is predominately molecular.

### 3.3.2. Kinematics of the Molecular Gas

The molecular gas in the disks of NGC 6670 forms two independent dynamical systems. In the channel maps (Fig. 7), the location of CO emission in each disk moves systematically from the west to the east. This is also clear in the radial velocity map (Fig. 10) that the velocity in each disk increases from the western end to the eastern end. In particular, the velocity of the stellar fuzzy feature in the southeastern end of NGC 6670E (§ 3.1) is consistent with the velocity distribution of the main body of NGC 6670E, which is most clear in Figure 6a (12'' to the east of the center) and in Figure 7 ( $v = 8760$  to  $8820$  km s<sup>-1</sup>). Together with the CO morphology shown in Figure 8a, the consistency of velocity suggests this fuzzy feature is part of the disk of NGC 6670E and not another galaxy.

The continuous change of CO velocity in the two galaxies as mentioned above and the double-peak line profiles of NGC 6670W (Fig. 9) suggest that the two molecular disks are both rotating. The CO  $p$ - $v$  diagram in Figure 6b shows the inner rotation curve of NGC 6670W. The CO emission has a relatively uniform distribution along a constant velocity gradient of  $\sim 60$  km s<sup>-1</sup> arcsec<sup>-1</sup> between  $8320$  and  $8860$  km s<sup>-1</sup> in the central 6'' (3.6 kpc) of the disk. In addition, in the channel maps (Fig. 7), one can find CO emission from the center of NGC 6670W in almost every channel between  $v = 8300$  and  $8840$  km s<sup>-1</sup>. The relatively uniform CO brightness over  $540$  km s<sup>-1</sup> suggests that the concentrated CO emission at the center of NGC 6670W in the integrated intensity map is the sum of CO in velocity space, rather than a concentration in true space.

In the outer regions of NGC 6670W, the CO rotation curve appears to become flat. The velocities of the flat portion of the rotation in the radial velocity map (Fig. 10) are  $8400$  and  $8740$  km s<sup>-1</sup> on the western and eastern side of the NGC 6670W disk respectively. This provides that the systemic velocity of NGC 6670W is  $8570$  km s<sup>-1</sup> and the maximum rotation velocity is  $170$  km s<sup>-1</sup>.

The constant velocity gradient in the inner 4 kpc of NGC 6670W has a velocity range which exceeds those observed in the outer portions of the galaxy. This suggests that some of the molecular gas in the inner part of NGC 6670W are on non-circular orbits. We suggest that the most natural explanation for this is a central molecular bar with a projected spatial extent of  $\lesssim 3.5$  kpc at a small angle ( $< 45^\circ$ ) with respect to the line of sight. Similar morphology in  $p$ - $v$  diagrams can be found in several other barred spiral galaxies, such as NGC 5746, NGC 5965 (Kuijken & Merrifield 1995), and NGC 4102 (Jogee & Kenny 1996). Theoretical studies have shown that stellar and gaseous bars may play an important role in driving gas into the central regions of galaxies (Schwarz 1984; Athanassoula 1992; Barnes & Hernquist 1991). Mihos & Hernquist (1996) further showed that the angular momentum of gas can be removed rapidly along a bar permitting intense gas inflow to take place. As suggested by the integrated CO flux, the central molecular bar in NGC 6670W may contain more than  $\sim 1.2 \times 10^{10} M_\odot$  of molecular gas. If the rapid inflow of molecular gas predicted by the simulations takes place in NGC 6670 as the merging process progresses, the center of NGC 6670W will become a powerful starburst region with a IR luminosity far exceeding the present value

The CO  $p$ - $v$  diagram of NGC 6670E (Fig. 6a) suggests the motion of the molecular gas is disturbed, as in the case of the H I gas (§ 3.2.2). As shown in Figure 6a, the  $p$ - $v$  diagram of CO emission along NGC 6670E’s major axis appears less symmetric than that of NGC 6670W. While the rotation curve appears to become flat on the eastern end of the disk, this is not as clearly observed on the western side. Thus the determination of the systemic and maximum rotation velocity is less certain. We use the averaged velocity in the innermost region to estimate the systemic velocity of NGC 6670E, which is  $8730 \text{ km s}^{-1}$ . Our best estimate of the maximum rotation speed is based on the velocity difference along the velocity gradient in the inner portion at the  $4\sigma$  level. The resultant value is  $\sim 100 \text{ km s}^{-1}$ . We note that, unlike NGC 6670W, the CO emission near the center of NGC 6670E is concentrated in both velocity and spatial extent (Fig. 6a). Thus the molecular concentration in the center of NGC 6670E seems more like a true concentration.

Figure 10 shows that the spin vectors of the two galaxies are both roughly toward the south. It also shows that, in this system, NGC 6670E is redshifted relative to NGC 6670W by  $160 \text{ km s}^{-1}$ . If the transverse velocities of both galaxies are small compared with the radial velocities, then the orbital vector of this system would also be toward the south. Such a configuration indicates a prograde-prograde interaction. Prograde-prograde encounters have been shown to be the most efficient at producing long tails (Toomre & Toomre 1972) and to have stronger gas inflow toward the nuclei of mergers (Mihos & Hernquist 1996). Although we cannot determine the true orbital motion of each galaxy without knowing the transverse velocities, a prograde-prograde geometry will give the best consistent explanation to the observed H I distribution and kinematics. We will further discuss this in § 4.1.3.

### 3.4. 20 cm Radio Continuum Results

The VLA 20 cm radio continuum map at  $3.1''$  resolution is shown in Figure 11. The one-dimensional profiles of 20 cm flux density and CO integrated intensity are also plotted in Figure 12 for comparison. Globally, the radio continuum emission is well correlated with both the CO emission and the optical emission. Two stronger radio continuum peaks appear at the eastern end of NGC 6670E and the western end of NGC 6670W (Fig. 12). The peak at the western end of NGC 6670W appears correlated with a bright region in the  $B$ -band image which may be a recent star forming region. The peak at the eastern end of NGC 6670E is roughly coincident with the heavily obscured region and may indicate recent embedded star formation activity.

The 20 cm emission in the center of each galaxy is marginally resolved by the  $3''.1$  circular beam along the major axis of each galaxy (Fig. 12). This suggests that the emission in each nucleus does not originate from a central point source such as an AGN, but originates from extended star forming regions. A similar suggestion for the energy source of the nuclear regions of NGC 6670 had been made based on the ISO mid-infrared observations (Hwang et al. 1999). The peak brightness in each

nucleus is  $10.3 \text{ mJy beam}^{-1}$  (607 K) in NGC 6670E and  $9.7 \text{ mJy beam}^{-1}$  (571 K) in NGC 6670W. The bright emission in the central regions of the galaxies implies that the strongest star formation activity occurs in the nuclear regions. Numerical simulations of interacting galaxies predict gas inflows into the nuclear regions and therefore anticipate a similar concentrated active star formation activity in the nuclear regions (Barnes & Hernquist 1991; Mihos, Bothun, & Richstone 1993; Mihos & Hernquist 1996).

Roughly 65% of the 20 cm flux of NGC 6670E and 50% of the flux of NGC 6670W originate from the inner 4 kpc region of each disk. The total flux density is 22.3 mJy for NGC 6670E, 35.6 mJy for NGC 6670W, and 60.4 mJy for the whole system. Furthermore, the 20 cm flux density and the far-infrared (FIR) flux density of NGC 6670 appear to obey the FIR–radio correlation of normal galaxies (galaxies without AGNs). The logarithmic FIR to radio flux density ratio defined by Condon, Anderson, & Helou (1991) is

$$q \equiv \log[(FIR/3.75 \times 10^{12}\text{Hz})/S_{1.49\text{GHz}}],$$

where the 20 cm flux density  $S_{1.49\text{GHz}}$  is in  $\text{W m}^{-2} \text{ Hz}^{-1}$ . The quantity  $FIR$  is defined as

$$FIR(\text{W m}^{-2}) \equiv 1.26 \times 10^{-14}(2.58S_{60\mu\text{m}} + S_{100\mu\text{m}}),$$

with the  $60\mu\text{m}$  flux density  $S_{60\mu\text{m}}$  and the  $100\mu\text{m}$  flux density  $S_{100\mu\text{m}}$  in Jy. Radio and FIR selected starbursts as well as optically selected spiral and irregular galaxies have a very narrow  $q$ -distribution ( $\sigma_q = 0.19$ ) centered on  $\langle q \rangle = 2.34$ . On the other hand, galaxies with radio emission powered by AGNs generally have  $q < 2$  (Condon 1992). Given  $S_{60\mu\text{m}} = 8.25 \text{ Jy}$ ,  $S_{100\mu\text{m}} = 15.2 \text{ Jy}$  (Moshir et al. 1990), and the measured  $S_{1.49\text{GHz}}$ , the value we find for  $q$  in NGC 6670 is 2.3. This is a strong indication that all the radio emission and infrared luminosity from NGC 6670 arise from star formation rather than AGN activity.

## 4. Discussion

### 4.1. The Dynamics of the Interaction

Our observations of NGC 6670 present the first example of an interacting system in which the H I disks have been highly perturbed but the individual stellar and molecular disks show relatively little distortion. The tidal tails of NGC 6670 only contains  $\sim 25\%$  of the total H I gas. NGC 6670 is among the few cases of interacting systems found to have a long (90 kpc) but less massive H I tail without obvious stellar counterparts. An extremely deep optical imaging is required to confirm the absence of stellar tails. Another system with similar H I and optical properties is NGC 3226/3227 (Mundell et al. 1995). The H I morphology and kinematics in NGC 6670 are also strikingly different from those of the molecular or stellar components.

In this section, we aim to explain the distribution and motion of atomic and molecular gas and to understand the dynamics of the interaction in this system. While there is no specific simulation



of NGC 6670, comparisons of our observation with the study of gravitational interaction of galaxies by Toomre & Toomre (1972)(hereafter TT72) can allow a fair amount of understanding of the interaction history and the orbital geometry of NGC 6670.

#### 4.1.1. *Masses of the Galaxies*

The dynamical mass within radius  $r$  in a galaxy can be estimated using

$$M(r) = r(v/\sin i)^2/G,$$

where  $i$  is the inclination angle of the disk and  $v$  is the projected rotation velocity of the disk. We chose the outermost radius of the stellar disk measured in the  $K'$ -band image for  $r$ , which is 12 kpc for NGC 6670W and 10 kpc for NGC 6670E. The rotational velocities are determined from the CO radial velocity (§ 3.3.2). Because  $i \sim 90^\circ$  for both galaxies, the dynamical masses are close to  $8.1 \times 10^{10} M_\odot$  for NGC 6670W and  $2.3 \times 10^{10} M_\odot$  for NGC 6670E.

In  $K'$ -band, the flux of NGC 6670W is 1.54 times greater than that of NGC 6670E (D.-C. Kim 2000, private communication). If the two galaxies have identical  $K'$ -band mass-to-light ratio and the dynamical mass of NGC 6670W should be reliable as its rotation is less perturbed, the  $K'$ -band light ratio implies the mass of NGC 6670E to be  $5.3 \times 10^{10} M_\odot$ , about twice the estimate above. The large difference between NGC 6670E’s dynamical mass and luminosity mass may suggest that the rotation of CO in NGC 6670E is too highly disturbed to be a good indicator of the dynamical mass.

#### 4.1.2. *Comparison of the Molecular and Atomic Gas Motion*

In interacting galaxy systems, the response of atomic and molecular gas to the tidal perturbation may be different. As the H I gas is generally distributed in the outer regions of spiral galaxies further beyond the stellar disks (Broeils & van Woerden 1994), it is less gravitationally bound to its host galaxies and is closer to the perturbing galaxy. Therefore the H I gas is more sensitive to tidal perturbation than the molecular gas that is mostly found in the inner regions of galaxies. H I clouds can more easily escape to form tails, bridges, or shells during the interaction.

The study of gas clouds in optically selected interacting galaxies (i.e., galaxies with stellar tails, bridges or other morphological peculiarity) have concentrated on the H I gas (e.g., the study of H I in a “Toomre Sequence” by Hibbard & van Gorkom (1996)). On the other hand, the study of molecular gas properties in merging galaxies have concentrated on advanced or late-stage mergers (e.g., Sanders et al. (1988); Scoville et al. (1991); Downes & Solomon (1998)). To date, there have been few studies containing observations of both molecular and atomic gas in early-stage interacting systems.

In NGC 6670, the response of molecular and atomic gas to the interaction is completely different even in the inner disk regions. While the molecular disks are still well separated and keep their identity of disk rotation, we can not tell two distinguished rotating H I systems from the  $p$ - $v$  diagram (Figure 6c). The H I disks are probably merging into a single rotating system dominated by the more massive galaxy NGC 6670W. This same trend is also observed in other interacting systems such as NGC 520 (Hibbard & van Gorkom 1996) and Arp 299 (Hibbard & Yun 1999), where the H I disks had already merged into a single system but the merging of stellar disks is still ongoing.

In NGC 6670W, the H I gas is likely in a rotating ring-like structure that has a rotation velocity slightly lower than that of the molecular disk (Fig. 6b). Much of the H I emission comes from the two outer ends of NGC 6670W’s stellar disk (the C and W concentrations). On the other hand, the strongest molecular emission in NGC 6670W is located in the circum-nuclear regions. The concentrated molecular clouds in its center appear to be in a bar elongated roughly along the line of sight, and the outer molecular disk appears to have a flat rotation curve, as shown in Figure 6b. Overall, the motion and distribution of the molecular clouds seem less perturbed in NGC 6670W, compared with those in NGC 6670E.

The CO(1–0) morphology, the CO velocity field, and the H I velocity field all suggest that the gravitational perturbation acts stronger on NGC 6670E than NGC 6670W. This is probably because NGC 6670W is more massive than NGC 6670E. The rotation of H I in NGC 6670E is almost unidentifiable in the H I  $p$ - $v$  diagram along its major axis (Fig. 6a). The H I  $p$ - $v$  diagram for NGC 6670E also shows some non-circular motion of H I, as described in § 3.2.2. While the original H I disk around NGC 6670E has nearly been destroyed, the molecular disk of NGC 6670E has not. As suggested by the CO  $p$ - $v$  diagram of NGC 6670E, the molecular clouds in the innermost of the galactic disk still rotate around the nucleus, while the flat outer part of its rotation curve on the western side appears disrupted. We also find that the CO rotation of NGC 6670E is highly perturbed by comparing its luminosity mass and dynamical mass. In addition, the CO emission from NGC 6670E seems more concentrated toward the nuclear region than in NGC 6670W. All the above may result from the tidal perturbation produced by the interaction.

#### 4.1.3. *Orbital Geometry and Interaction History*

There are several important results in the study of TT72 that can be used to infer the orbital geometry and the interaction history of NGC 6670. 1) Only a prograde passage with orbital inclination  $i \lesssim 30^\circ$  with respect to the spin plane of the perturbed galaxy can produce long tidal tails. 2) Tidal tails can only be generated after the galaxies have passed their pericenters. 3) During the prograde encounter, only particles orbiting their host galaxies with radii greater than 0.5 pericentric distance can be ejected to form tidal tails if the interacting pair have comparable masses.

Our VLA observation reveals an H I tail of 90 kpc in extent. According to the first point from TT72, the interaction in NGC 6670 must be prograde for at least one of the galaxies. The CO velocity field reveals that the galaxies have similar direction of spin. Therefore the interaction should be a prograde-prograde encounter. This is also suggested by the CO systemic velocity of each galaxy and the global velocity of the H I disks (Fig. 6c). Furthermore, besides the short NE tail extending in the N-S direction, most of the H I in this system is distributed along the E-W direction. This suggests that the orbital plane of the interacting galaxies in NGC 6670 lies nearly parallel to the plane defined by the line of sight and the E-W direction, and the transverse velocities in the N-S direction are small. These are all consistent with the hypothesis of a prograde-prograde interaction.

The second point from TT72 mentioned above states that the galaxies have already finished their first approach and have been interacting with each other for at least long enough to produce a 90 kpc tail. We can estimate the pericentric distance of this system by noting that there are no significant stellar tails detected in optical and NIR images. According to the third point mentioned from TT72, if there were significant stellar components orbiting either galaxy with radii greater than 0.5 pericentric distance, we should see a stellar tail in this system. This gives a lower limit for the pericentric distance. Therefore the extent of NGC 6670W’s stellar disk in the optical images is the lower limit for the pericentric distance,  $\sim 25$  kpc. With such a large impact parameter, only the extended H I disk has formed tails. This also explains why NGC 6670 has relatively less H I distributed along the tails compared with other systems like NGC 4676 or Arp 244 (§ 3.2.1) which may have had smaller pericentric distances in their most recent encounters. We conclude that the difference in appearance between the H I and stellar-plus-molecular components in NGC 6670 can be ascribed to a relatively large impact parameter and the different initial distribution of those components.

It is worth to point out that the present projected separation of the galaxies (16 kpc) is less than the lower limit of the previous pericentric distance (25 kpc). This suggests either that the separation of the galaxies along the line of sight is larger than  $\sim 20$  kpc, or that the galaxies are during their next close encounter which should have a smaller pericentric distance. The following discussion prefers the second case.

NGC 6670 (and also NGC 3226/3227, (Mundell et al. 1995)) demonstrates that H I tails can form independently of stellar tails. The formation of H I tails without stellar counterparts might be a common phenomenon for early stage mergers with large pericentric distances. On the other hand, in this kind of interacting systems, the stellar tails can still form in their later stage of merging. Since the H I tails and probably also the disrupted dark halo are carrying part of the galaxies’ angular momentum, the galaxies should have a smaller pericentric distance during their next close encounter than the previous one. If there are stars located outside the radius of 0.5 pericentric distance during the next encounter, they will likely be ejected to form stellar tails. It is also possible to form new minor H I tails during future encounters. Such minor tidal features forming in later encounters can be found in the simulations. Due to the different initial distribution

of stellar and gaseous components, different tidal features made of stars or gas could be generated after a few orbital periods. By the same token, the observed offset or morphological inconsistency between stellar and gaseous tails/bridges in many other interacting systems (e.g., the M81 group, Yun, Ho, & Lo (1994); Arp 299, Hibbard & Yun (1999)) might be explained by the different initial distributions of the different components. Simulations by Mihos (2001) had already verified this suggestion.

The interaction age of NGC 6670 can also be estimated if we know the true spatial velocity ( $V$ ) of the tails. Given the projected 90 kpc extension of the W tail, the time elapsed since this tail began forming must be at least 90 kpc/ $V$ . Consider that the tails are escaping particles that became nearly gravitationally unbound to the host galaxies due to the tidal force of the interaction (TT72). Thus we assume that the escaping particles were not accelerated to higher velocities during the encounter but have velocities comparable to their original velocities prior to the interaction. Therefore, the value of  $V$  can be estimated as the rotation velocity plus orbital velocity of a galaxy. We use the value  $\Delta V/2 + v$  for  $V$ , where  $v$  is the rotational velocity of W tail’s parent galaxy and  $\Delta V$  is relative radial velocity of the galaxies. Given that the rotational velocities of the galaxies are 100 and 170 km s<sup>-1</sup> and  $\Delta V = 160$  km s<sup>-1</sup>, the possible  $V$  ranges between 180 and 250 km s<sup>-1</sup>. Thus the age of the tail is  $\sim 4 \times 10^8$  yr. The age of the tail can perhaps be used to indicate the age of interaction. Similar dating methods were used on other interacting systems (e.g., (Hibbard & Yun 1999; Murphy 2000)). The interaction age of the advanced merger Arp 299 was estimated to be  $7.5 \times 10^8$  yr (Hibbard & Yun 1999). This is almost twice the interaction age of NGC 6670. Although there is an uncertainty (probably a factor of 2) with this kind of age estimate, it is still plausible that NGC 6670 is in an early stage of merging.

In addition to the age of interaction, we can also estimate the orbital time scale of this system using  $\pi R/\Delta V$  where  $R$  is projected nuclear separation and  $\Delta V$  is relative radial velocity between the galaxies. Given  $R = 16$  kpc, the orbital time scale is  $\sim 3 \times 10^8$  yr. This time scale is comparable with the interaction age. It is therefore possible that the second approach of the galaxies are now ongoing if the galaxies are in gravitationally bound orbits. Furthermore, as described in § 3.2.1, the H I C concentration may cause the extinction in the eastern side of the disk of NGC 6670W. This implies that the C concentration is in front of NGC 6670W along the line of sight. Moreover, the lack of obscuration in the western part of NGC 6670E suggests that NGC 6670E is in front of the C concentration and therefore is in front of NGC 6670W. If this is the case, the galaxies must be approaching to each other because NGC 6670W is blueshifted relative to NGC 6670E.

We can estimate the ratio of the kinetic and potential energies of this system to test whether the two disks are gravitationally bound. The ratio is

$$T/|U| \approx (M_r \Delta V^2/2)/(GM_E M_W/R) = R\Delta V^2/(2G(M_E + M_W)),$$

where  $M_r$  is the reduced mass of the system,  $\Delta V$  is the relative velocity and  $R$  is the nuclear separation of the galaxies with masses  $M_E$  and  $M_W$ . For NGC 6670W, we use the dynamical mass,  $8.1 \times 10^{10} M_\odot$ . For NGC 6670E, we use the luminosity mass  $5.3 \times 10^{10} M_\odot$  as described in

§ 4.1.1. Using the projected nuclear separation (16 kpc) for  $R$  and the radial velocity difference (160 km s<sup>-1</sup>) for  $\Delta V$ , we estimate the ratio  $T/|U|$  to be 0.35. Because both  $\Delta V$  and  $R$  used here are lower limits, this estimate  $T/|U|$  is also a lower limit. Although we cannot obtain an upper limit for  $T/|U|$ , it is reasonable to conclude that the galaxies are gravitationally bound ( $T/|U| < 1$ ) for three reasons. 1) The masses we use are lower limits because they only include material within the stellar distribution. The inclusion of material outside the extent of the stellar disks would make the ratio  $T/|U|$  smaller. 2) As described in the previous paragraph, the interaction age is comparable with the orbital time scale. If the galaxies were unbound, they would have a much larger separation than the present projected separation after an orbital time scale since the first encounter. The relatively small projected separation suggests the galaxies to be bound, unless the separation along the line of sight is very large. 3) As suggested by the relative line-of-sight geometry of NGC 6670E, the C concentration, and NGC 6670W, the galaxies are approaching each other again. This can only happen when the galaxies are gravitationally bound.

In addition, the formula above for  $T/|U|$  can be used to better constrain the galaxies' transverse velocities perpendicular to the line of sight. The relative velocity ( $\Delta V$ ) of the galaxies at the previous pericenter can be estimated by using the lower limit of the pericentric distance (25 kpc) for  $R$  and assuming  $T/|U| = 1$ . The estimated relative velocity is 210 km s<sup>-1</sup>. This is slightly larger than the present radial velocity difference of the galaxies (160 km s<sup>-1</sup>). Because the galaxies' relative velocity reached its maximum at the pericenter, the 210 km s<sup>-1</sup> estimated above must be an upper limit for the present relative velocity. Therefore, the observed radial velocity difference suggests that the transverse velocity must be small compared to the radial velocity. This is consistent with the discussion at the beginning of this section.

In conclusion, the galaxies in NGC 6670 are likely in gravitationally bound prograde-prograde orbits with an orbital plane nearly edge-on along the E-W direction. The galaxies have already passed through a pericenter at least once. The pericentric distance of the first close encounter is greater than the diameter of each stellar disk, therefore no strong stellar tails were generated during that encounter. We summarize the discussed orbital geometry in Figure 13. The above general picture of the interaction in NGC 6670 is self-consistent, but it should be verified by numerical simulations.

#### 4.1.4. *H I Concentration between the Stellar Disks*

Our H I observations reveal a massive atomic gas concentration (the C concentration) in the overlap region between the two stellar disks. The C concentration has an H I mass of  $\sim 2 \times 10^9 M_\odot$ . In some systems of intermediate merging stage such as Arp 244 (Stanford et al. 1990; Lo et al. 2000; Gao et al. 2001), Arp 299 (Sargent & Scoville 1991; Aalto et al. 1997; Casoli et al. 1999), and NGC 6090 (Gao et al. 1999; Bryant & Scoville 1999), CO images reveal massive molecular gas reservoirs ( $> 10^9 M_\odot$ ) in the disk overlap regions which seem to be the most active star forming areas and could dominate the overall starburst activity (Wynn-Williams et al. 1991; Zhou, Wynn-Williams,

& Sanders 1993; Mirabel et al. 1998).

As indicated in § 3.2.2, the H I velocities of the E and W concentrations match the CO velocities of the eastern side of NGC 6670E and the western side of NGC 6670W, respectively. This suggests that these two H I concentrations are remnants of the outer H I disks of the galaxies and still have velocities similar to the rotation velocities of the inner disks. In contrast, Figure 6 shows that the C concentration has a velocity range between the CO velocities of the western side of NGC 6670E and the eastern side of NGC 6670W. The spatial location and anomalous velocity of the C concentration could be explained by either direct cloud-cloud collisions of H I between the prograde-prograde disks, or a superposition of two independent H I components whose velocities are slowed down by the tidal potential (§ 3.2.2). We note that, even for the second case, cloud-cloud collisions may still take place in the future because the galaxies are now approaching each other. Jog & Solomon (1992) showed that H I cloud-cloud collisions in colliding galaxies can produce a hot ionized over-pressure remnant gas to compress the GMCs and lead to starbursts in off-nuclear regions. The observed concentration of H I between the two disks of NGC 6670 may provide support to the starburst mechanism proposed by Jog & Solomon (1992).

Numerical simulations do not generally produce gas concentrations in the disk overlap regions during the early or intermediate stages of merging (Arp 244 for example, Mihos, Bothun, & Richstone (1993)). Our H I observations of NGC 6670 provide a possible evolutionary link to the intermediate-stage mergers with molecular gas concentration in the disk overlap regions, like in Arp 244, Arp 299 and NGC 6090. The C concentration in NGC 6670 has an H I gas mass comparable to the molecular concentrations found in the disk overlap regions of other LIRGs. Knowing that the C concentration is massive and the galaxies are still approaching each other, we expect that during the future interaction, more H I gas (and even molecular gas) will flow into this region and get trapped. After the gas density increases, a conversion of H I into H<sub>2</sub> may occur. It is possible that the H I C concentration is the progenitor of the molecular concentration in the disk overlap regions observed in some late stage LIRGs.

#### 4.2. Is NGC 6670 Undergoing Starbursts?

Both galaxies in NGC 6670 have signatures which are anticipated by numerical simulations to be important for fueling the nuclear starbursts. Our BIMA CO observations reveal that the molecular gas in NGC 6670E is concentrated toward its nuclear region. A molecular bar is suggested in the center of NGC 6670W via the CO  $p$ - $v$  diagram (Fig. 6b), which can efficiently drive gas into the nuclear region (Mihos & Hernquist 1996). The IR luminosity of NGC 6670, of  $3.8 \times 10^{11} L_{\odot}$  implies a high star formation rate of many tens of solar masses per year. Furthermore, the total molecular gas mass revealed by our observations is also high ( $3.6 \times 10^{10} M_{\odot}$ ). However, it is possible that the GMCs of NGC 6670 are forming stars with an efficiency similar to the GMCs in the Galactic disk. If this is the case, the high infrared luminosity of NGC 6670 would be merely due to the large reservoirs of molecular gas, similar to the nonstarburst LIRG Arp 302 (Lo, Gao, & Gruendl 1997).

Therefore, it is important to determine whether the star formation activity in the large molecular reservoirs of NGC 6670 are really elevated to starburst levels.

#### 4.2.1. The Star Formation Efficiency

There are several ways to probe starbursts. If the infrared luminosity is entirely due to dust heated by recent star formation, the star formation rate (SFR) would be directly proportional to the infrared luminosity. Various conversions between infrared luminosity and star formation rate have been suggested, from  $\text{SFR} (M_{\odot} \text{ yr}^{-1}) \sim 77 \text{ to } 300 \times 10^{-12} L_{\text{IR}}(L_{\odot})$  (Scoville & Young 1983; Gallagher & Hunter 1986; Hunter et al. 1986; Inoue, Hirashita, & Kamaya 2000). Thus the global star formation rate for NGC 6670 is *sim*30 to 120  $M_{\odot} \text{ yr}^{-1}$ . This implies a molecular gas depletion time between  $10^8$  and  $10^9$  yr, comparable with the orbital time scale of NGC 6670 and the typical galaxy-galaxy merging time scale for gas-rich mergers demonstrated in most simulations.

The ratio  $\text{SFE} \equiv L_{\text{IR}}/M_{\text{H}_2}$  is often used to indicate the star formation efficiency (SFR per unit molecular gas mass). The mean SFE for the GMCs in the Milky Way’s disk is  $\sim 4 L_{\odot}/M_{\odot}$  (Scoville & Good 1989). For nearby starburst galaxies, the value of SFE is  $\sim 10 L_{\odot}/M_{\odot}$  (Sanders & Mirabel 1996). For nuclear starburst regions in LIRGs, the SFE ranges from 20 to greater than 100  $L_{\odot}/M_{\odot}$  (Scoville et al. 1991; Bryant & Scoville 1999). The global SFE for NGC 6670 is  $\sim 10 L_{\odot}/M_{\odot}$ .

In order to investigate the location and spatial extent of the starburst, the correlation between the FIR and radio continuum flux densities (see, e.g., Condon, Anderson, & Helou (1991)) can be applied to the individual galaxies of NGC 6670. This should be a good approximation for NGC 6670 because we have shown that the system as a whole obeys the FIR–radio correlation and that the radio continuum emission of NGC 6670 is not from AGN activity (§ 3.4). After scaling the infrared luminosity with the 20 cm flux density (Table 2), we find an SFE of 12.7  $L_{\odot}/M_{\odot}$  for NGC 6670E and 8.8  $L_{\odot}/M_{\odot}$  for NGC 6670W. The SFE of NGC 6670E is significantly higher than that of the GMCs in the Galactic disk but is not as high as the SFE of nuclear starbursts in LIRGs.

In normal galaxies, the FIR–radio correlation appears to hold locally within individual galaxies and the FIR and radio morphologies are similar (Bicay et al. 1988; Condon 1992; Marsh & Helou 1995; Lu et al. 1996). This is also the case in NGC 6670, as the radio continuum and mid-infrared morphology observed by ISO are similar (Hwang et al. 1999). If we assume the distribution of FIR emission is similar to that of the radio continuum, the strong radio emission from the nuclei of NGC 6670 would imply that the nuclear regions are the sites of current star formation activity. We plot one-dimensional profiles of 20 cm flux density and CO integrated intensity along the major axes of the two disks in Figure 12. It shows that the ratio of 20 cm flux density to CO integrated intensity is significantly higher in the center of NGC 6670E compared to other regions in NGC 6670E or NGC 6670W. Thus, the SFE in the center of NGC 6670E is higher than the mean SFE of NGC 6670E or the whole NGC 6670 system.

To quantify the SFE in the nuclear regions, we use two methods to estimate the 20 cm and CO flux from the central regions. 1) We fit the nuclear components of both galaxies in the high resolution CO integrated intensity map and the 20 cm map with 2D Gaussians. Using this method, we obtain SFEs of 17 and 10  $L_{\odot}/M_{\odot}$  for the nuclear regions of NGC 6670E and NGC 6670W, respectively. 2) We directly sum the pixels within the inner 4 kpc ( $\sim 7''$ ) regions of both galaxies in the 20 cm map and the high resolution CO intensity map to obtain the flux. The resulting SFE is 18  $L_{\odot}/M_{\odot}$  for the nucleus of NGC 6670E and 11 for the nucleus of NGC 6670W. Table 3 summarizes the parameters given by the two methods described above.

The SFE estimated above is likely to be a lower limit, since the molecular mass may be over-estimated by using a CO-to-H<sub>2</sub> conversion factor  $X$  derived from the Milky Way disk (§ 3.3.1). We conclude that the nucleus of NGC 6670E is a starburst region and its star formation efficiency is at least four times higher than that of the GMCs in the Milky Way disk.

#### 4.2.2. Other Indicators

We can calculate the peak CO brightness temperature ( $T_b$ ) using the channel maps. In order to minimize the effect of beam dilution, we use the highest resolution maps which include B array data only. For a  $1.8''$  ( $\sim 1.1$  kpc) beam, the highest CO brightness in NGC 6670E appears in its center, in the channel of  $v = 8740$  km s<sup>-1</sup>. This brightest component is unresolved and has a peak brightness temperature of 4.5 K. In NGC 6670W, several peaks with  $T_b$  of 3 to 3.5 K appear in the disk and we cannot distinguish an isolated peak in its center. In the starburst galaxy M82, the molecular clouds smaller than 100 pc have  $T_b$  ranging from 13 to 34 K (Shen & Lo 1995). At the same time, the highest  $T_b$  observed by Rickard et al. (1977) with a  $65''$  single dish beam ( $\sim 1$  kpc) on M82 is 0.6 K. The single dish beam size of Rickard et al. (1977) is comparable with the synthesis beam used here for NGC 6670. Compared with those M82 data, the brightness temperature in the center of NGC 6670E and NGC 6670W is unusually high. Although our resolution is insufficient to resolve individual clouds, this still suggests that the molecular clouds in the centers of both NGC 6670E and NGC 6670W are very bright and may have properties similar to the clouds in the starburst regions of M82.

We estimate the average infrared surface brightness of the nuclear regions using the FIR–radio correlation to scale the IR emission with 20 cm radio continuum flux. Assuming that all the nuclear 20 cm flux given by the Gaussian fit comes from the area within one full-width-half-maximum (FWHM, see Table 3), we estimate the mean IR surface brightness to be  $2.4 \times 10^4$  and  $2.0 \times 10^4$   $L_{\odot}$  pc<sup>-2</sup> for the  $\sim 2$  kpc nuclear regions of NGC 6670E and NGC 6670W, respectively. The typical IR surface brightness of resolved starburst regions of few hundred pc sizes in M82, NGC 253 and other LIRGs is  $\sim 10^5$   $L_{\odot}$  pc<sup>-2</sup> (see Lo et al. (1987) for a summary). In the Orion molecular cloud (OMC 1) near the Trapezium, the mean radiation field strength is  $\sim 2 \times 10^5$   $L_{\odot}$  pc<sup>-2</sup> (Tielens & Hollenbach 1985). The mean values for the inner parts of NGC 6670 are roughly 10 times smaller. Because our 20 cm beam size ( $\sim 2$  kpc) is several times larger than the sizes of



other resolved starbursts ( $< 1$  kpc), the FWHMs given by the fitting are clearly upper limits for the sizes of the nuclear star forming regions in NGC 6670. Therefore, the mean value of  $\sim 2 \times 10^4 L_{\odot} \text{ pc}^{-2}$  obtained over  $\sim 2$  kpc scale is high and the IR surface brightness in the nuclear regions of NGC 6670 may be comparable with those in other starburst regions.

The measured CO brightness temperature and IR surface brightness are both largely limited by the resolution and only represent lower bounds to the actual values. However, they qualitatively provide tests on the molecular gas properties and the radiation flux coming from young massive stars. They both indicate that the nuclei of NGC 6670E and NGC 6670W are undergoing higher than normal levels of star formation, perhaps even at the level of starbursts. This is consistent with the star formation efficiency estimated in § 4.2.1.

#### 4.2.3. *What Produced the Elevated SFE?*

In NGC 6670, all the indicators discussed above suggest that the nuclei have properties similar to other starburst regions. IN NGC 6670E, the observed accumulation of molecular gas in the central  $\sim 2$  kpc region may be responsible for the elevated star formation activity. The detailed accumulation mechanism, however, is not clear. The optical, H I, and CO observations all show distorted morphologies. The kinematics of the atomic and molecular gas are also disturbed. It appears that the tidal interaction has disturbed the gas and stars in the disk of NGC 6670E. On the other hand, in the center of NGC 6670W, much of the molecular gas appears to be in a central molecular bar but the star formation efficiency is not as high as in the nucleus of NGC 6670E. It is unclear in our observations why the intense bar driven gas inflow predicted by the simulations does not take place in NGC 6670W. With that NGC 6670E has higher kinematic disturbance and star formation efficiency than those of NGC 6670W, our observations appear to support the hypothesis that the starburst is fueled by the gas inflow due to the tidal perturbation produced by the interaction of the galaxies.

In recent simulations of Mihos & Hernquist (1996), the starburst history in merging disk galaxies sensitively depends on the structure of the progenitor galaxies. Collisions between disk/halo galaxies produce gas inflows shortly after the first close passage and thus produce starbursts while the galaxies are still widely separated. On the other hand, collisions between disk/bulge/halo galaxies can only produce strong gas inflows and starbursts in the final stage of the mergers. Our observations of NGC 6670 show that starbursts can be triggered when the galaxies are still widely separated, which according to Mihos & Hernquist (1996) would imply that the NGC 6670 galaxies fit the disk/halo type. However, bulges of the two galaxies clearly exist in the NIR images (Fig 1). Our observations do not appear to well agree with the model. Similarly, there is another ULIRG found to be in an early stage of merging and also have a bulge (IRAS 01521+5224, (Murphy 2000)). To further confirm the structural dependence predicted by the simulations, observations of the structures of the NGC 6670 galaxies as well as other early stage LIRGs are needed.

## 5. Summary

1. Very long H I tidal tails in NGC 6670, a pair of two overlapping edge-on galaxies, are revealed by our VLA observations, which proves that the two galaxies are interacting gravitationally. We have compared the morphology and motion of H I in NGC 6670 with the studies of Toomre & Toomre (1972) to reconstruct a self-consistent orbital geometry for this interacting system. The interaction is prograde-prograde with an orbital plane nearly edge-on in the E-W direction, with the galaxy spin vectors and orbital vectors essentially all parallel to each other. The galaxies appear to be in an early stage of merging, and have already passed a pericenter roughly  $\sim 4 \times 10^8$  yr ago. Their pericentric distance of the previous encounter is at least 25 kpc. The galaxies are most likely gravitationally bound and are probably approaching another close encounter.

2. The total H I mass in the NGC 6670 system is  $1.6 \times 10^{10} M_{\odot}$ . Unlike other intermediate or late stage mergers, only 25% of NGC 6670's H I gas is distributed within the tails. Most of the H I in this system was found near the two stellar disks. The H I disks of the galaxies are interacting with each other and have slower rotational velocities than those of the CO disks. The global H I kinematics appears to be dominated by the rotation of the more massive galaxy NGC 6670W. The H I near NGC 6670W appears to be in a rotating ring-like structure. The H I disk of NGC 6670E has been nearly destroyed by the interaction and the H I motion near NGC 6670E appears to be highly perturbed.

3. Three apparent H I gas concentrations have been identified at the edges of the stellar disks. The most massive one, the C concentration, is located in the region between the stellar disks and has a collective H I mass of  $2 \times 10^9 M_{\odot}$ . The C concentration might be a true concentration formed due to collisions of H I clouds, but a superposition of two spatially separated components is also possible. We need higher resolution H I data to resolve this ambiguity. This H I concentration may be accumulating more H I gas and molecular gas during the future interaction of the galaxies, to become the next site of starburst in this system.

4. BIMA CO(1–0) observations reveal large molecular gas reservoirs in NGC 6670. The molecular gas mass is  $1.1 \times 10^{10} M_{\odot}$  for NGC 6670E and  $2.5 \times 10^{10} M_{\odot}$  for NGC 6670W. The molecular clouds in both galaxies are concentrated toward the nuclear regions, especially in NGC 6670E. A large portion of the CO flux in NGC 6670E and in NGC 6670W comes from the inner 4 kpc regions of the galaxies. The estimated face-on molecular gas column density of each galaxy is  $\sim 10^3 M_{\odot} \text{ pc}^{-2}$ , larger than the value of the Galactic center (40–300  $M_{\odot} \text{ pc}^{-2}$ ) but smaller than other LIRGs ( $> 10^4 M_{\odot} \text{ pc}^{-2}$ ) in advanced merging stages. The rotation curve of NGC 6670W suggests that there may exist a molecular bar in the inner disk. Both molecular disks exhibit normal rotational signatures. The kinematics and morphology of the molecular disks in the two galaxies appear less disturbed than the H I disks, probably due to their greater resistance to tidal disruption.

5. Our VLA 20 cm radio continuum imaging reveals the distribution of the radio continuum emission from the galaxies. The 20 cm flux density and FIR flux density of NGC 6670 appear to

obey the FIR–radio correlation for normal galaxies so AGN activity is ruled out in this system. In each galaxy, more than 50% of the radio continuum flux comes from the inner 4 kpc region. This suggests active star formation in the nuclear regions of the galaxies.

6. The FIR–radio correlation was applied locally to the galaxies’ nuclear regions. We estimate the star formation efficiency of the central regions of both galaxies by scaling the FIR luminosity by the radio continuum flux. The nuclei of NGC 6670E and NGC 6670W are estimated to have the values of SFE  $\sim 18$  and  $\sim 11 L_{\odot}/M_{\odot}$ , respectively. Those values are significantly larger than typical SFEs of GMCs in the Galactic disk ( $\sim 4 L_{\odot}/M_{\odot}$ ) and are nearly as high as that found in starbursts and in other LIRGs (20 to  $>100 L_{\odot}/M_{\odot}$ ). The star formation efficiency and other indicators of starbursts such as high CO brightness temperature and FIR surface brightness all suggest that the central regions of the two galaxies have properties similar to starburst regions in other galaxies.

We thank D.-C. Kim and D.B. Sanders for the use of the  $K'$ -band image of NGC 6670. We would like to thank the referee of ApJ Letters, Pierre-Alan Duc, for his invaluable comments and suggestions that have greatly helped to improve this paper. We are also very grateful to the referee of AJ, Tom Murphy, for his kindly providing an alternative interpretation to our H I data and the very useful comments. W.H. Wang and K.Y. Lo acknowledge partial support from the Academia Sinica and the National Science Council in Taiwan. K.Y. Lo, Yu Gao and Robert Gruendl acknowledge partial support from the Laboratory of Astronomical Imaging which is funded by NSF grant AST 96-13999 and by the University of Illinois. This study of NGC 6670 was started when W.H. Wang was a master degree student in the Institute of Astronomy in National Central University. W.H. Wang thanks the support from NCU. Yu Gao is grateful to the ASIAA for its hospitality during a short visit when the writing of this paper was initiated.

### A. CGCG 301-032

We detect H I emission at the velocity range between 8630 and 8870  $\text{km s}^{-1}$  from the galaxy CGCG 301-032 (IRASF 18335+5949), which is  $\sim 5'$  away in the southeast of NGC 6670. The low resolution H I integrated intensity map and velocity map of CGCG 301-032 are plotted in Figure 14. There is no H I detected between NGC 6670 and CGCG 301-032 under the current detection limit. The H I integrated flux of CGCG 301-032 obtained from the low resolution channel maps is 1.6  $\text{Jy km s}^{-1}$  and indicates the total H I gas mass to be  $5.5 \times 10^9 M_{\odot}$ . The extent of the HI gas is about 30 kpc. The galaxy’s H I velocity gradient along NE-SW direction shows that the H I of CGCG 301-032 is in a rotating disk. The large amount of atomic gas and the H I rotating feature suggest that CGCG 301-032 is a relatively small (12 kpc in optical extent) early-type spiral galaxy. However, the spiral arms are not apparent in the DSS image and our  $J$ -band image. This galaxy is also detected in our 20 cm radio continuum map. The total flux density of CGCG 301-032 at 20 cm is 5.9 mJy.

## REFERENCES

- Aalto, S., Radford, S. J. E., Scoville, N. Z., & Sargent, A. I. 1997, *ApJ*, 475, L107
- Arp, H. 1996, *ApJS*, 14, 1
- Athanassoula, E. 1992, *MNRAS*, 259, 345
- Barnes, J. E., & Hernquist, L. 1991, *ApJ*, 370, 65
- Bessell, M.S., Castelli, F., & Plez, B. 1998, *A&A*, 333, 231
- Bicay, M. D., Helou, G., & Condon J. J. 1988, *ApJ*, 338, L53
- Broeils, A. H., & van Woerden, H. 1994 *A&AS*, 107, 129
- Briggs, D. S. 1995, *BAAS*, 187, 112.02
- Bryant, P. M., & Scoville, N. Z. 1999, *AJ*, 117, 2632
- Bushouse, H. A. 1987, *ApJ*, 320, 49
- Bushouse, H. A., Werner, M. W., & Lamb, S. A. 1988, *ApJ*335, 74
- Casoli, F., Willaime, M.-C., Viallefond, F., & Gerin, M. 1999, *A&A*, 346, 663
- Condon, J. J., Anderson, M. L., Helou, G. 1991, *ApJ*, 376, 95
- Condon, J. J., Huang, Z.-P., Yin, Q. F., & Thuan, T. X. 1991, *ApJ*, 378, 65
- Condon, J. J. 1992, *ARA&A*, 30, 575
- Downes, D., & Solomon, P. M. 1998, *ApJ*, 507, 615
- Duc, P. A., Mirabel, I. F., & Maza, J. 1998, *A&AS*, 124, 533
- Gallagher, J. S., Hunter, D. A. 1986, in *Conf. Proc. of Star Formation in Galaxies, Pasadena 1986*, ed. C. Lonsdale (Washington, DC: GPO), 167
- Gao, Y. 1996, Ph.D. thesis, State Univ. of New York at Stony Brook
- Gao, Y., Gruendl, R., Lo, K. Y., Hwang, C. Y., Veilleux, S. 1997, in *AIP Conf. Ser. 393, Star Formation Near and Far: Seventh Astrophysics Conference*, ed. S. S. Holt & L. G. Mundy. (New York: AIP Press), 319
- Gao, Y., Gruendl, R. A., Hwang, C. Y., Lo, K. Y. 1999, in *IAU Symp. 186, Galaxy Interactions at Low and High Redshift*, ed. J. E. Barnes, & D. B. Sanders, (Dordrecht: Kluwer), 227
- Gao, Y., & Solomon, P. M. 1999, *ApJ*, 512, L99

- Gao, Y., Lo, K. Y., Lee, S.-W., & Lee, T.-H. 2001, *ApJ*, 548, 172
- Genzel, R. et al. 1998, *ApJ*, 498, 579
- Hibbard, J. E., & van Gorkom, J. H. 1996, *AJ*, 111, 655
- Hibbard, J. E., & Yun, M. S. 1999, *AJ*, 118, 162
- Huchtmeier, W. K., & Richter, O.-G. 1989, *A General Catalog of H I Observations of Galaxies* (New York: Springer-Verlag)
- Hunter, D. A., Gillett, F. C., Gallagher, J. S., Rice, W. L., & Low, F. J. 1986, *ApJ*, 303, 171
- Hwang, C.-Y., Lo, K. Y., Gao, Y., Gruendl, R. A., & Lu, N. Y. 1999, *ApJ*, 511, L17
- Inoue, A. K., Hirashita, H. & Kamaya, H. 2000, *PASJ*, 52, 539
- Jog, C. J., & Solomon, P. M. 1992, *ApJ*, 387, 152
- Jogee, S., & Kenny, J. D. P. 1996, in *ASP Conf. Ser. 91, Barred Galaxies*, ed. R. Buta, D. A. Crocker, & B. G. Elmegreen (San Francisco: ASP), 230
- Joseph, R. D., & Wright, G. S. 1985, *MNRAS*, 214, 87
- Kennicutt, R. C., Jr., Keel, W. C., van der Hulst, J. M., Himmel, E., & Roettiger, K. A. 1987, *AJ*, 93, 1011
- Kennicutt, R. C., Jr. 1998, *ApJ*, 498, 541
- Kuijken, K., & Merrifield, M. R. 1995, *ApJ*, 443, L13
- Lo, K. Y., Cheung, K. W., Masson, C. R., Phillips, T. G., Scott, S. L., & Woody, D. P. 1987, *ApJ*, 312, 574
- Lo, K. Y., Gao, Y., & Gruendl, R. A. 1997, *ApJ*, 475, L103
- Lo, K. Y., Hwang, C. Y., Lee, S. W., Kim, D. C., Wang, W. H., Lee, T. H., Gruendl, R., Gao, Y. 2000, in *ASP Conf. Ser. 197, Dynamics of Galaxies: from the Early Universe to the Present*, ed. F. Combes, G. A. Mamon, & V. Charmandaris (Paris: ASP), 279
- Lu, N. Y., Helou, G., Tuffs, R., Xu, C., Malhotra, S., Werner, M. W., & Thronson, H. 1996, *A&A*, 315, L153
- Maloney, P., & Black, J. H. 1988 *ApJ*, 325, 389
- Marsh, K. A., & Helou, G. 1995, *ApJ*, 445, 599
- Martin, J. M., Bottinelli, L., & Gouguenheim, L. 1991, *A&A*, 245, 393

- Meixner, M., Young Owl, R. C. & Leach, R. 1999, *PASP*, 111, 997
- Melnick, J., & Mirabel, I. F. 1990, *A&A*, 231, L19
- Mihos, J. C., Bothun, G. D., & Richstone, D. O. 1993 *ApJ*, 418, 82
- Mihos, J. C., & Hernquist, L. 1996, *ApJ*, 464, 641
- Mihos, J. C. 2001, *ApJ*, in press
- Mirabel, I. F. et al. 1998, *A&A*, 333, L1
- Moshir, M. et al. 1990, *IRAS Faint Source Catalogue*, version 2.0
- Mundell, C. G., Pedlar, A., Axon, D. J., Meaburn, J., & Unger, S. W. 1995, *MNRAS*, 277, 641
- Murphy, T. W., Arnus, L., Matthews, K., Soifer, B. T., & Mazzarella, J. M., et al. 1996, *AJ*, 111, 1025
- Murphy, T. W. 2000, Ph.D. thesis, California Institute of Technology
- Regan, M. W., & Gruendl, R. A. 1995, in *ASP Conf. Proc. Ser. 77, Astronomical Data Analysis Software and Systems IV*, ed. R. A. Shaw, H. E. Payne, & J. J. E. Hayes (San Francisco: ASP), 335
- Rickard, L. J., Palmer, P., Morris, M., Turner, B. E., & Zuckerman, B. 1977, *ApJ*, 213, 673
- Rieke, G. H., Cutri, R., Black, J. H., Kailey, W. F., McAlary, C. W., Lebofsky, M. J., & Elston, R. 1985, *ApJ*, 290, 116
- Roberts, M. S. 1975, in *Galaxies and the Universe*, ed. A. Sandage, M. Sandage, & J. Kristian (Chicago: University of Chicago Press), 309
- Sanders, D. B., Solomon, P. R., & Scoville, N. Z. 1984, *ApJ*, 276, 182
- Sanders, D. B., Soifer, B. T., Elias, J. H., Madore, B. F., Matthews, K., Neugebauer, G., & Scoville, N. Z. 1988, *ApJ*, 325, 74
- Sanders, D. B., Scoville, N. Z., & Soifer, B. T. 1991, *ApJ*, 370, 158
- Sanders, D. B., Egami, E., Lipari, S., Mirabel, I. F., Soifer, B. T. 1995, *AJ*, 110, 1993
- Sanders, D. B., & Mirabel, I. F. 1996, *ARA&A*, 34, 749
- Sargent, A. I., & Scoville, N. Z. 1991, *ApJ*, 366, L1
- Sault, R. J., Teuben, P. J., & Wright, M. C. H. 1995, in *ASP Conf. Proc. 77, Astronomical Data Analysis Software and Systems IV*, ed. R. A. Shaw, H. E. Payne, & J. J. E. Hayes (San Francisco: ASP), 433

- Schwarz, M. P. 1984, MNRAS, 209, 93
- Scoville, N., & Young, J. S. 1983, ApJ, 265, 148
- Scoville, N. Z., Sanders, D. B., & Clemens, D. P. 1986, ApJ, 310, L77
- Scoville, N. Z., Yun, M. S., Clemens, D. P., Sanders, D. B., & Walker, W. H. 1987, ApJS, 63, 821
- Scoville, N. Z., & Good, J. 1989, ApJ, 339, 140
- Scoville, N. Z. et al. 1991, ApJ, 366, L5
- Shen, J., & Lo, K. Y. 1995, ApJ, 445, L99
- Smith, H. E., Lonsdale, C. J., Lonsdale, C. J., & Diamond, P. J. 1998, ApJ, 493, L17
- Solomon, P. M., Downes, D., & Radford, S. J. E. 1992, ApJ, 387, L55
- Solomon, P. M. et al. 1997, ApJS, 478,144
- Spinoglio, L., Malkan, M. A., Rush, B., Carrasco, L., & Recillas-Cruz, E. 1995, ApJ, 453, 616
- Stanford, S. A., Sargent, A. I., Sanders, D. B., & Scoville, N. Z. 1990, ApJ, 349, 492
- Taniguchi, Y., & Ohyama, Y. 1998, ApJ, 509, L89
- Tielens, A. G. G. M., & Hollenbach, D. 1985, ApJ, 291, 747
- Toomre, A., & Toomre, J. 1972, ApJ, 178, 623 (TT72)
- Tully, R. B., Pierce, M. J. 2000, ApJ, 533, 744
- Hulst, J. M. van der 1979, A&A, 71, 131
- van Driel, W., Gao, Y., & Monnier-Ragaigne, D. 2001, A&A, in press
- Welch, W. J., et al. 1996, PASP, 108, 93
- Wynn-Williams, C. G., Eales, S. A., Becklin, E. E., Hodaap, K.-W., Joseph, R. D., McLean, I. S.,  
Simons, D. A., & Wright, G. S. 1991, ApJ, 377, 426
- Young, J. S., & Knezek, P. M. 1989, ApJ, 347, L55
- Young, J. S., & Scoville, N. Z. 1991, ARA&A, 29, 581
- Yun, M. S., Ho, P. T. P., & Lo, K. Y. 1994, Nature, 372, 530
- Yun, M. S., & Scoville, N. Z. 1995, ApJ, 451, L45
- Zhou, S., Wynn-Williams, C. G., & Sanders, D. B. 1993, ApJ, 409, 149

Zwicky, F. 1971, Catalogue of Selected Compact Galaxies and of Post-Eruptive Galaxies (Guemligen, Switzerland: F. Zwicky)



Fig. 1.— A comparison of the optical to near-infrared images of NGC 6670 at  $B, V, R, I, J,$  and  $K'$ -bands.

Fig. 2.— Robustly weighted H I moment maps at  $18'' \times 15''.6$  resolution of NGC 6670. (a) The H I integrated intensity contours are overlaid on the  $J$ -band grey-scale image. The contour levels are 1.5, 6, 10, 15, 20, 25, 30, 40, 50, and 60 times  $8.5 \text{ mJy beam}^{-1} \text{ km s}^{-1}$  which corresponds to an H I column density of  $3.3 \times 10^{19} \text{ cm}^{-2}$ . Several H I components mentioned in the text are labeled. (b) The H I intensity-weighted radial velocity contours on H I integrated intensity grey-scale image. The velocity difference between all adjacent contours is  $40 \text{ km s}^{-1}$ .

Fig. 3.— Uniformly weighted H I integrated intensity at  $11''.4$  resolution of NGC 6670. The H I intensity is plotted with grey contours and the CO(1–0) integrated intensity is also plotted with black contours for comparison. The H I contour levels are 2, 4, 6, ..., 24 times  $18 \text{ mJy beam}^{-1} \text{ km s}^{-1}$  which corresponds to an H I column density of  $1.5 \times 10^{20} \text{ cm}^{-2}$ . The underlying grey-scale picture is the  $K'$ -band image of D.-C Kim and D. B. Sanders.

Fig. 4.— H I spectra of the whole NGC 6670 system, the W tail, the NE tail, and the C concentration. The spectrum of the C concentration is obtained from the high resolution cube. Others are obtained from the low resolution cube.

Fig. 5.— H I channel map contours at  $18'' \times 15''.6$  resolution, overlaid on the  $J$ -band grey-scale image. Contours start at  $0.69 \text{ mJy beam}^{-1}$  ( $2\sigma$ ) and increase by steps of  $0.69 \text{ mJy beam}^{-1}$ . Plotted in the upper-left corner of each sub-plot is the central heliocentric velocity of the channel.

Fig. 6.— H I and CO position-velocity ( $p$ - $v$ ) diagrams: (a) along the optical disk of NGC 6670E (P.A.=  $120^\circ$ ), (b) along the optical disk of NGC 6670W (P.A.=  $70^\circ$ ), (c) along the line connecting the two nuclei of NGC 6670E and NGC 6670W (P.A.=  $76^\circ$ ). The H I  $p$ - $v$  diagrams obtained from the low resolution cube are plotted with thin lines filled with grey colors. The H I contours shown in all the three plots represent H I brightness starting at  $0.7 \text{ mJy beam}^{-1}$  ( $2\sigma$ ) and increasing by steps of  $0.7 \text{ mJy beam}^{-1}$ . The grey color is smoothed H I brightness. In the three plots, CO  $p$ - $v$  diagrams made along the same position angles as H I are plotted with thick lines. The CO  $p$ - $v$  diagrams were obtained from the low resolution cube. The CO contour levels are 1, 2, 3, ..., 7 times  $26 \text{ mJy beam}^{-1}$  ( $1.8\sigma$ ). In (a), the origin of the position axis is at the center of NGC 6670E. In (b) and (c), the origins are at the center of NGC 6670W. The cross signs in each plot represent the H I (thin lines) and CO (thick lines) resolutions in both velocity and spatial axes. The velocity resolution is  $21.8 \text{ km s}^{-1}$  for H I and is  $20 \text{ km s}^{-1}$  for CO. The spatial resolutions for H I and CO are determined from the beam sizes along the direction of the slices and change slightly in each plot. The central positions of the H I W concentration, the C concentration, and the E concentration are indicated with horizontal grey lines in (a) and (b). The central velocities of NGC 6670E and NGC 6670W are indicated with vertical grey lines. The scales in both axes are different in all the three plots.

Fig. 7.— CO(1–0) channel map contours at  $2''.7 \times 2''.1$  resolution overlaid on the grey-scale  $K'$ -band image. The contour levels are 1, 2, 3, 4, and 5 times  $26 \text{ mJy beam}^{-1}$  ( $= 2\sigma = 0.4 \text{ K}$ ). The central velocity of each channel is labeled in the upper-right corner of every sub-plot.

Fig. 8.— CO(1–0) integrated intensity maps. (a) Intensity map at  $5''.4 \times 4''.6$  resolution. The CO integrated intensity is plotted as contours overlaid on the  $K'$ -band image provided by D.-C. Kim and D.B. Sanders. Contour levels are 1, 2, 3, 4, 6, 8, 10, 12, 14, 18, 22, and 26 times  $2.2 \text{ Jy beam}^{-1} \text{ km s}^{-1}$ . (b) Intensity map at  $2''.7 \times 2''.1$  resolution. The CO intensity contours are overlaid on the  $B$ -band grey-scale image. The contour levels are 1, 2, 3, 4, 6, 8, and 10 times  $2.4 \text{ Jy beam}^{-1} \text{ km s}^{-1}$  ( $= 1.1 \times 10^{22} \text{ cm}^{-2}$ ).

Fig. 9.— CO(1–0) spectra of NGC 6670E and NGC 6670W obtained from the higher resolution channel maps.

Fig. 10.— CO radial velocity contours derived from the low resolution intensity-weighted radial velocity map, overlaid on the grey-scale CO integrated intensity. The contours are plotted every  $30 \text{ km s}^{-1}$ .

Fig. 11.— 20 cm radio continuum contours of NGC 6670 overlaid on (a) grey-scale of the  $B$ -band optical image and (b) grey-scale of the high resolution CO(1–0) integrated intensity. The contours in each sub-plot are 1, 2, 4, 8, 16, 32, 64, and 128 times  $0.1 \text{ mJy beam}^{-1}$  ( $= 2\sigma = 5.4 \text{ K}$ ). The black circles represent the 20 cm beam and the grey ellipse represents the CO beam.

Fig. 12.— CO(1–0) integrated intensity and 20 cm radio continuum intensity profiles along the major axes of NGC 6670W (P.A. =  $70^\circ$ ) and NGC 6670E (P.A. =  $120^\circ$ ). The CO intensity is plotted with solid lines and the 20 cm intensity is plotted with dashed lines. The 20 cm intensity is labeled in the left-hand-side of each plot. The CO intensity is labeled in the right-hand-side of each plot. In each plot, the zero of the x-axis is located in the center of the galaxy.

Fig. 13.— A cartoon depiction of a possible orbital geometry of NGC 6670. Two major ideas of this cartoon discussed in § 4.1.3 are 1) the galactic planes and the orbital plane are all viewed nearly edge-on 2) NGC 6670E is in front of NGC 6670W along the line of sight. The radial systemic velocities of the galaxies ( $V_{sys}$ ) are shifted so that NGC 6670W has zero radial velocity. The rotational velocities ( $V_{rot}$ ) are determined from the CO velocity field. We note that the orbital geometry presented by this cartoon is consistent with the observations but is not necessarily the unique possibility. Numerical simulations are needed to verify this orbital geometry.

Fig. 14.— Contours of the low resolution H I intensity and radial velocity of CGCG 301-032. (a) Integrated H I intensity contours at 1.5, 6, 10, 15, 20, 25, 30, 40, and 50 times  $8.5 \text{ mJy beam}^{-1} \text{ km s}^{-1}$  ( $3.3 \times 10^{19} \text{ cm}^{-2}$ ), overlaid on a  $J$ -band image. (b) radial velocity contours overlaid on the grey-scale H I integrated intensity. The contours are plotted every  $25 \text{ km s}^{-1}$ .

Table 1. Observed H I Properties of NGC 6670

HI Component	$S_{21\text{cm}}^{\text{a}}$ (Jy km s <sup>-1</sup> )	$M_{\text{HI}}$ ( $10^9 M_{\odot}$ )	$\langle\sigma_v\rangle^{\text{b}}$ (km s <sup>-1</sup> )	$n_{\text{HI,peak}}/\langle n_{\text{HI}}\rangle^{\text{c}}$ ( $10^{20}$ atoms cm <sup>-2</sup> )	$l_{\text{max}} \times l_{\text{min}}^{\text{d}}$ (kpc $\times$ kpc)
NGC 6670 (total) <sup>1</sup>	4.83	16.4	...	...	110 $\times$ 30
W tail <sup>1</sup>	0.97	3.3	16.5	5.1 / 2.8	60 $\times$ 20
NE tail <sup>1</sup>	0.24	0.8	10.7	3.9 / 2.5	15 $\times$ 15
C concentration <sup>2</sup>	0.57	2.0	34.5	> 24.0 / 14.0	14 $\times$ 13
W concentration <sup>2</sup>	0.40	1.4	34.9	> 38.0 /	unresolved

<sup>1</sup>Properties of the extended H I components are derived from the low resolution (robustly weighted) maps.

<sup>2</sup>Properties of the concentrated components are derived from the high resolution (uniformly weighted) maps.

<sup>a</sup>Integrated H I line flux obtained from the channel maps.

<sup>b</sup>H I mean velocity dispersion derived from the intensity-weighted velocity dispersion maps.

<sup>c</sup>Peak and averaged H I column density derived from the integrated intensity maps.

<sup>d</sup>Maximum and minimum dimensions measured from the first outer contours in the integrated intensity maps.

Table 2. Global CO and Radio Continuum Properties of NGC 6670

Derived Parameter	NGC 6670E	NGC 6670W
$S_{\text{CO}}^{\text{a}}$ (Jy km s <sup>-1</sup> )	65.4	149.7
$M_{\text{H}_2}$ ( $10^{10} M_{\odot}$ )	1.1	2.5
$n_{\text{H}_2, \text{peak}}^{\text{b}}$ ( $10^{22}$ molecules cm <sup>-2</sup> )	8.0	11.8
$N_{\text{H}_2, \text{peak}}^{\text{b}}$ ( $10^3 M_{\odot}$ pc <sup>-2</sup> )	1.3	1.9
$S_{20\text{cm}}$ (mJy)	22.3	35.6
$L_{\text{IR}}^{\text{c}}$ ( $10^{11} L_{\odot}$ )	1.4	2.2
SFE <sup>d</sup> ( $L_{\odot}/M_{\odot}$ )	12.7	8.8

<sup>a</sup>CO integrated flux obtained from the high resolution channel maps.

<sup>b</sup>Peak edge-on H<sub>2</sub> column density derived from the high resolution intensity map.

<sup>c</sup>IR luminosity calculated by scaling the total IR luminosity with the 20 cm flux. See § 4.2.1.

<sup>d</sup>Star formation efficiency  $\equiv L_{\text{IR}}/M_{\text{H}_2}$ . See § 4.2.1.

Table 3. Properties of the Nuclear Regions of NGC 6670

Derived Parameter	Center of NGC 6670E	Center of NGC 6670W
By Gaussian Fit		
$L_{\text{IR}}$ ( $10^{10} L_{\odot}$ )	9.5	12.6
$\Sigma_{\text{IR}}^{\text{a}}$ ( $10^4 L_{\odot} \text{ pc}^2$ )	2.4	2.0
$M_{\text{H}_2}$ ( $10^9 M_{\odot}$ )	5.6	12.5
SFE ( $L_{\odot}/M_{\odot}$ )	17	10
$l_{\text{maj}} \times l_{\text{min}}^{\text{b}}$ (kpc $\times$ kpc)	$2.5 \times 2.0$	$3.4 \times 2.3$
By Direct Measuring		
$L_{\text{IR}}$ ( $10^{10} L_{\odot}$ )	9.0	10.5
$M_{\text{H}_2}$ ( $10^9 M_{\odot}$ )	5.0	9.4
SFE ( $L_{\odot}/M_{\odot}$ )	18	11

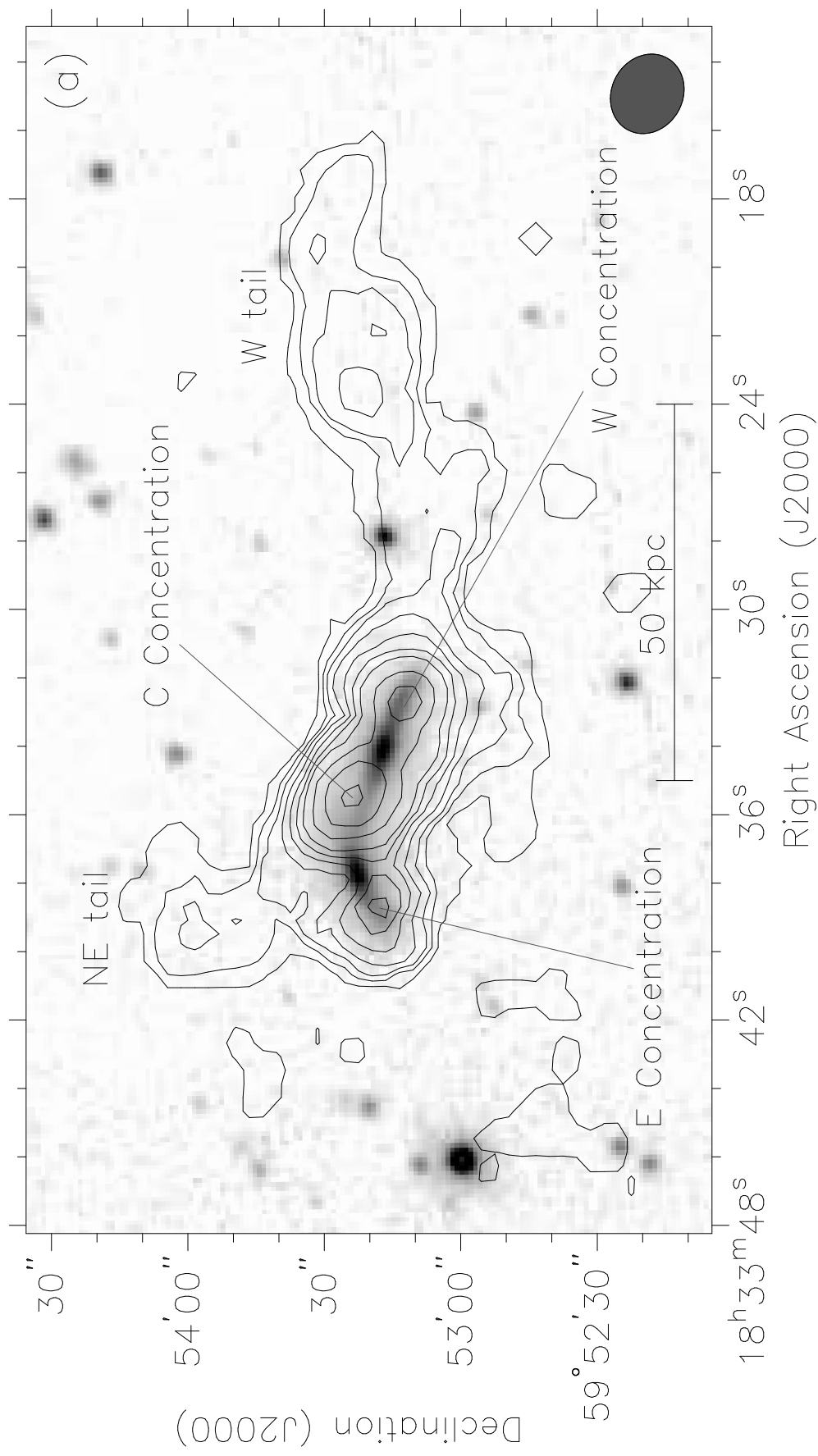
<sup>a</sup>Averaged infrared surface brightness.

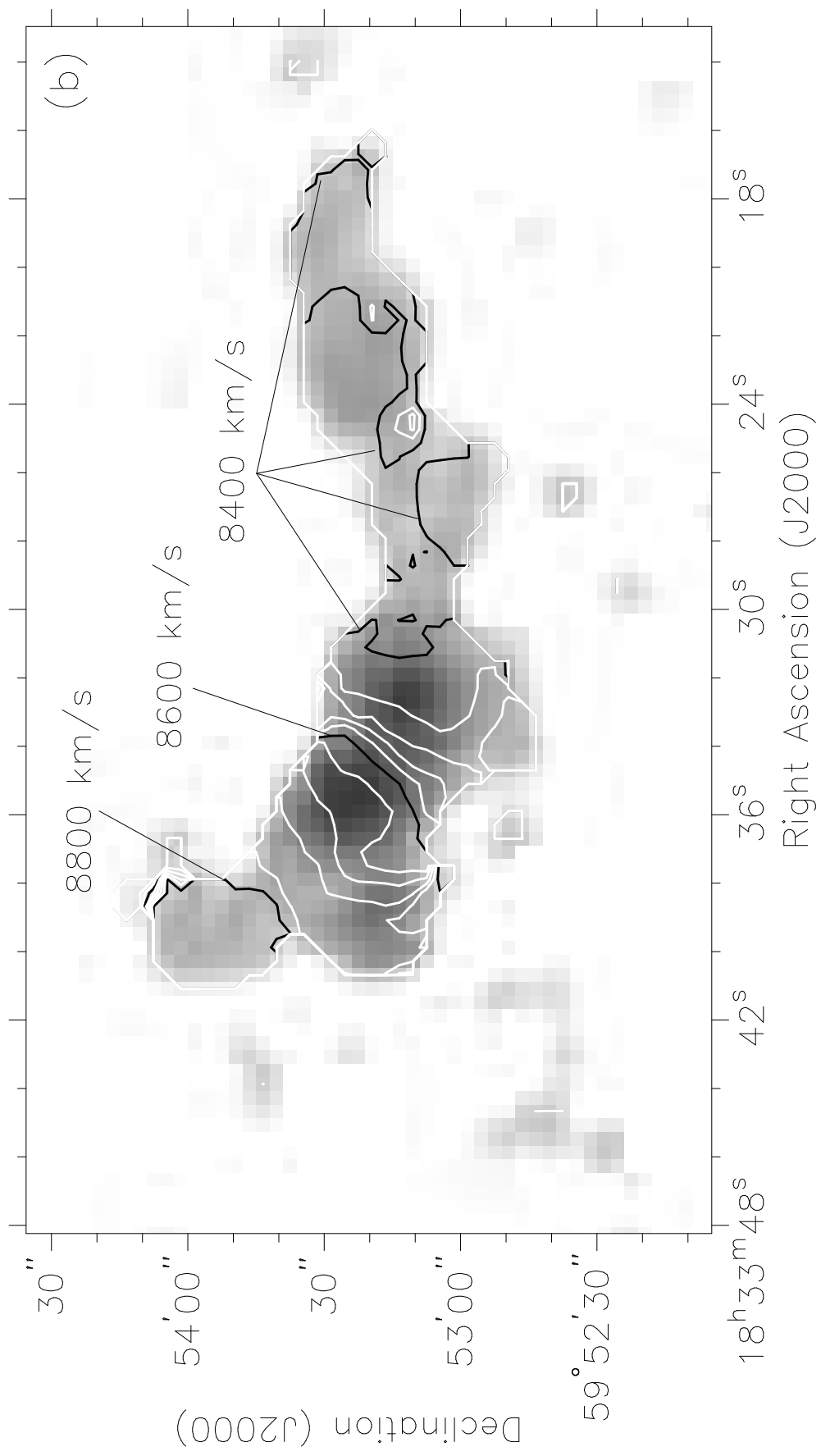
<sup>b</sup>Major and minor axes FWHMs given by the Gaussian fit in the 20 cm map.

Note. — This table summarizes the properties of the nuclear regions. The CO and 20 cm flux from each galactic nucleus was isolated by 1) applying Gaussian fit to the nuclear regions 2) directly summing the pixels within the inner  $4 \text{ kpc} \times 4 \text{ kpc}$  regions. Also see the text in § 4.2.1.

This figure "fig1.jpg" is available in "jpg" format from:

<http://arxiv.org/ps/astro-ph/0103280v1>







This figure "fig3.jpg" is available in "jpg" format from:

<http://arxiv.org/ps/astro-ph/0103280v1>

This figure "fig4.jpg" is available in "jpg" format from:

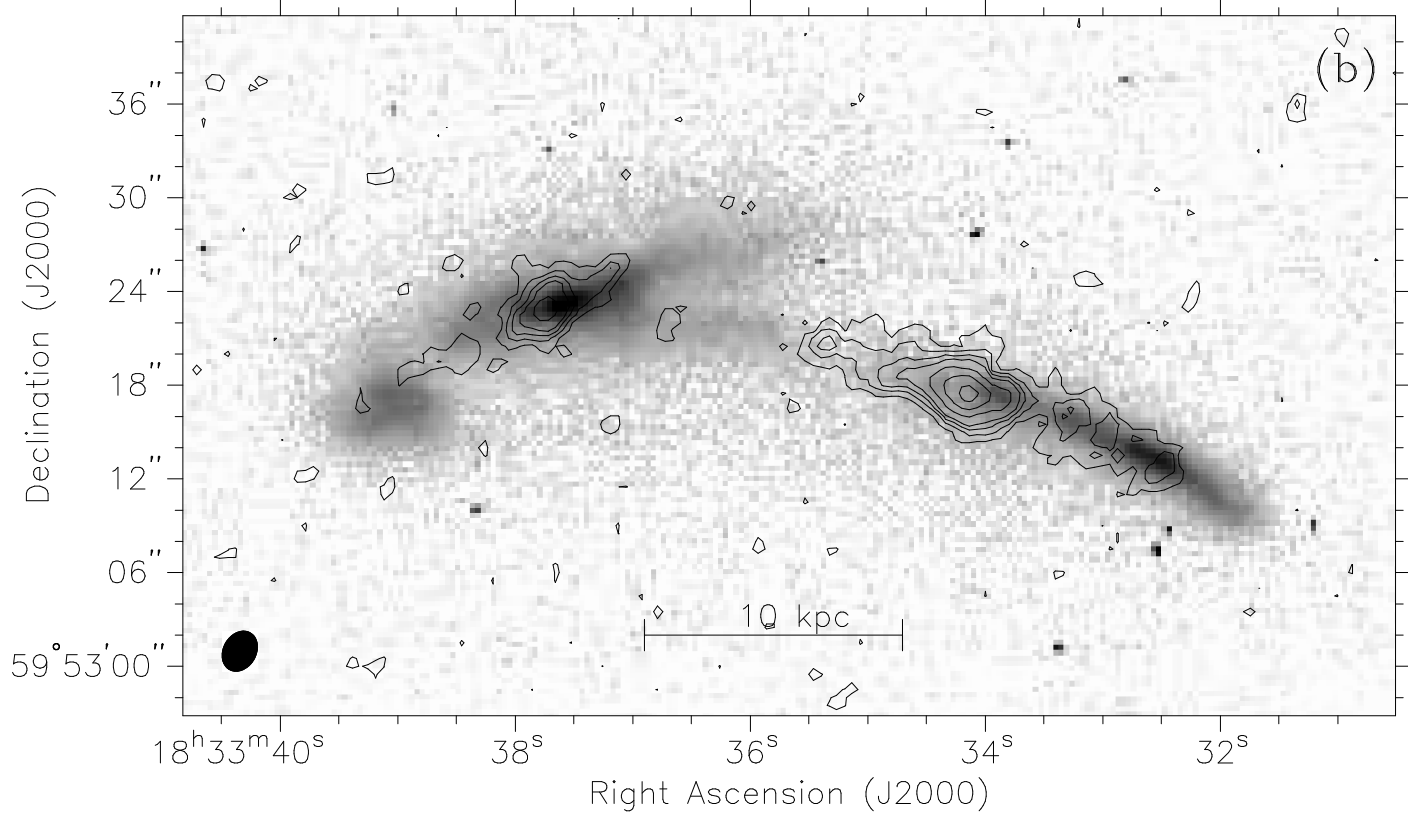
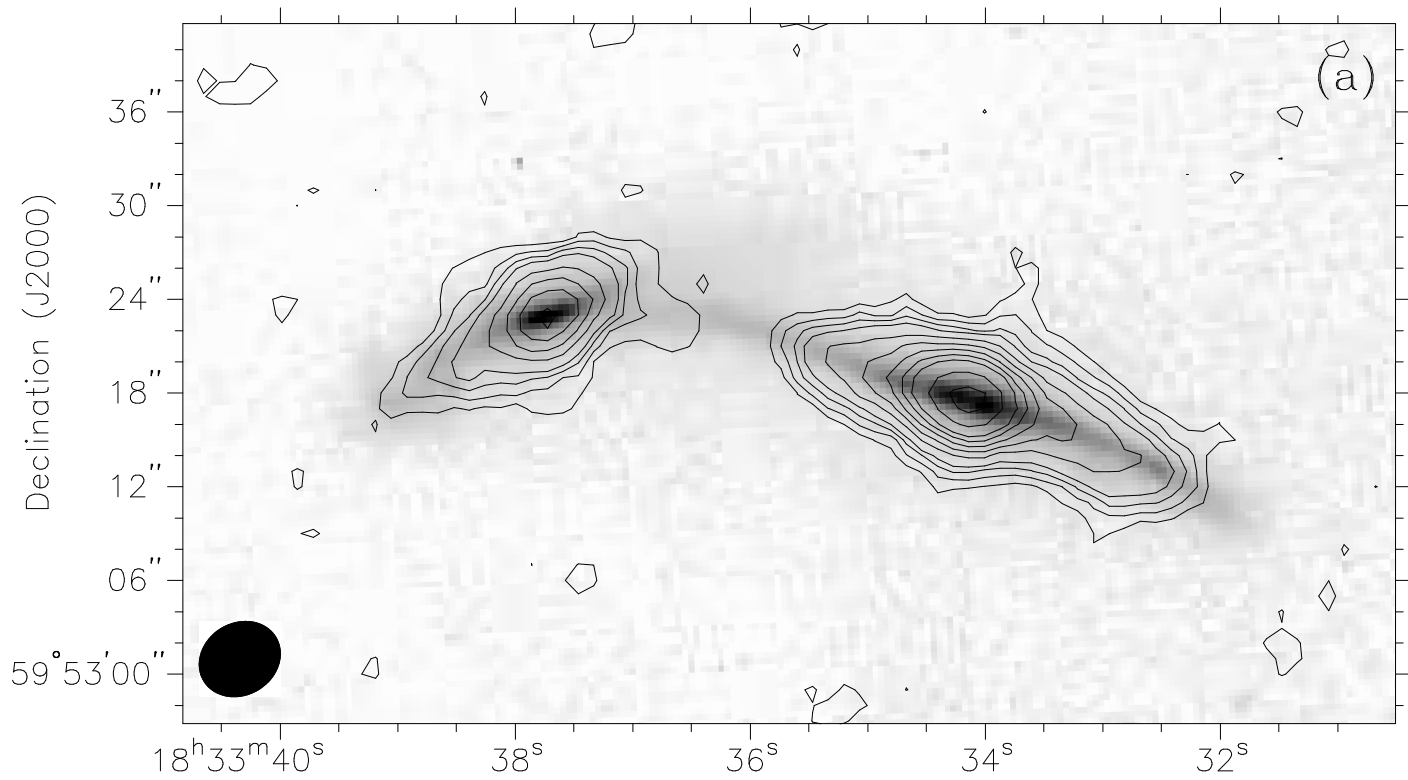
<http://arxiv.org/ps/astro-ph/0103280v1>

This figure "fig5.jpg" is available in "jpg" format from:

<http://arxiv.org/ps/astro-ph/0103280v1>

This figure "fig6.jpg" is available in "jpg" format from:

<http://arxiv.org/ps/astro-ph/0103280v1>

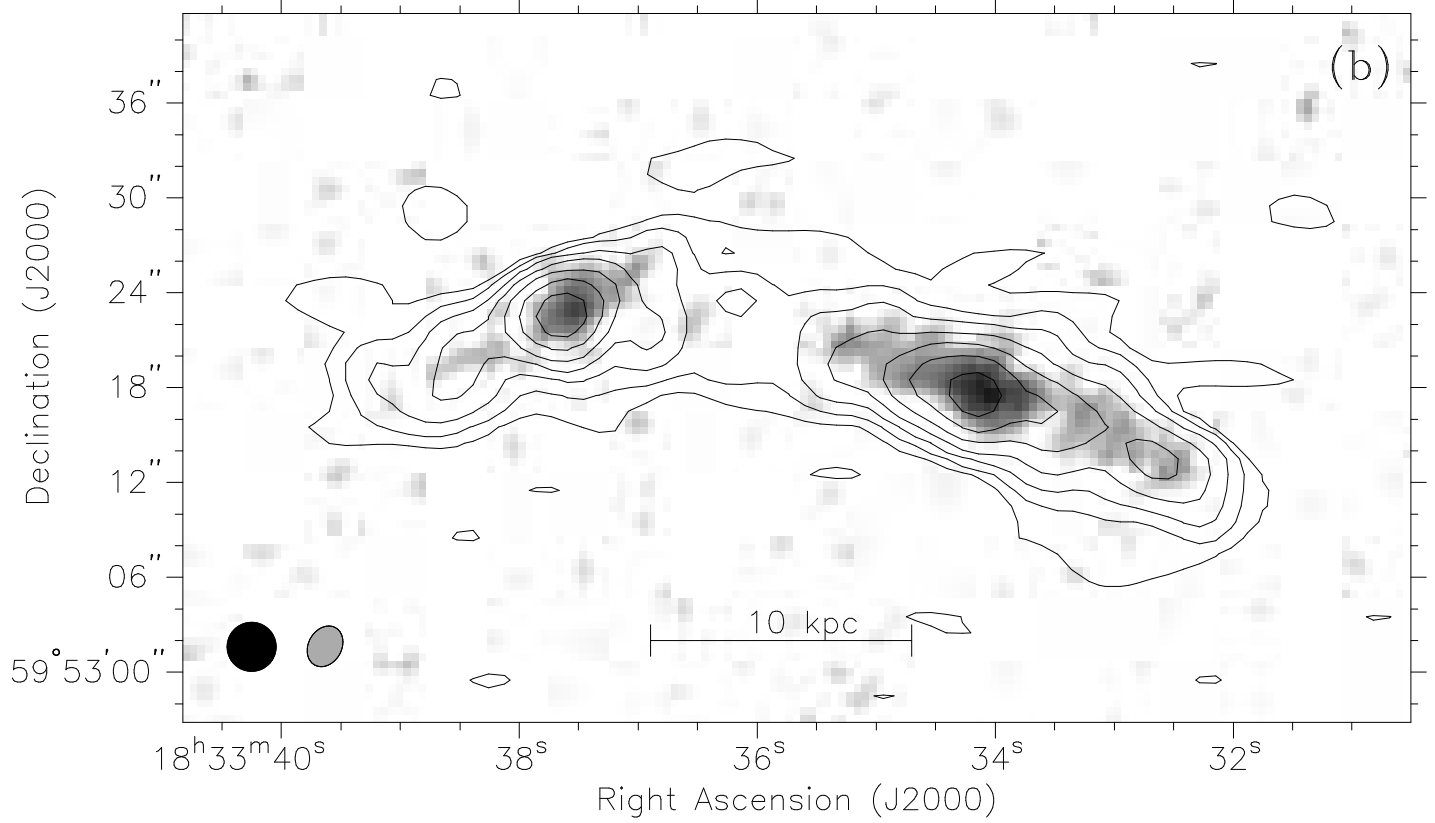
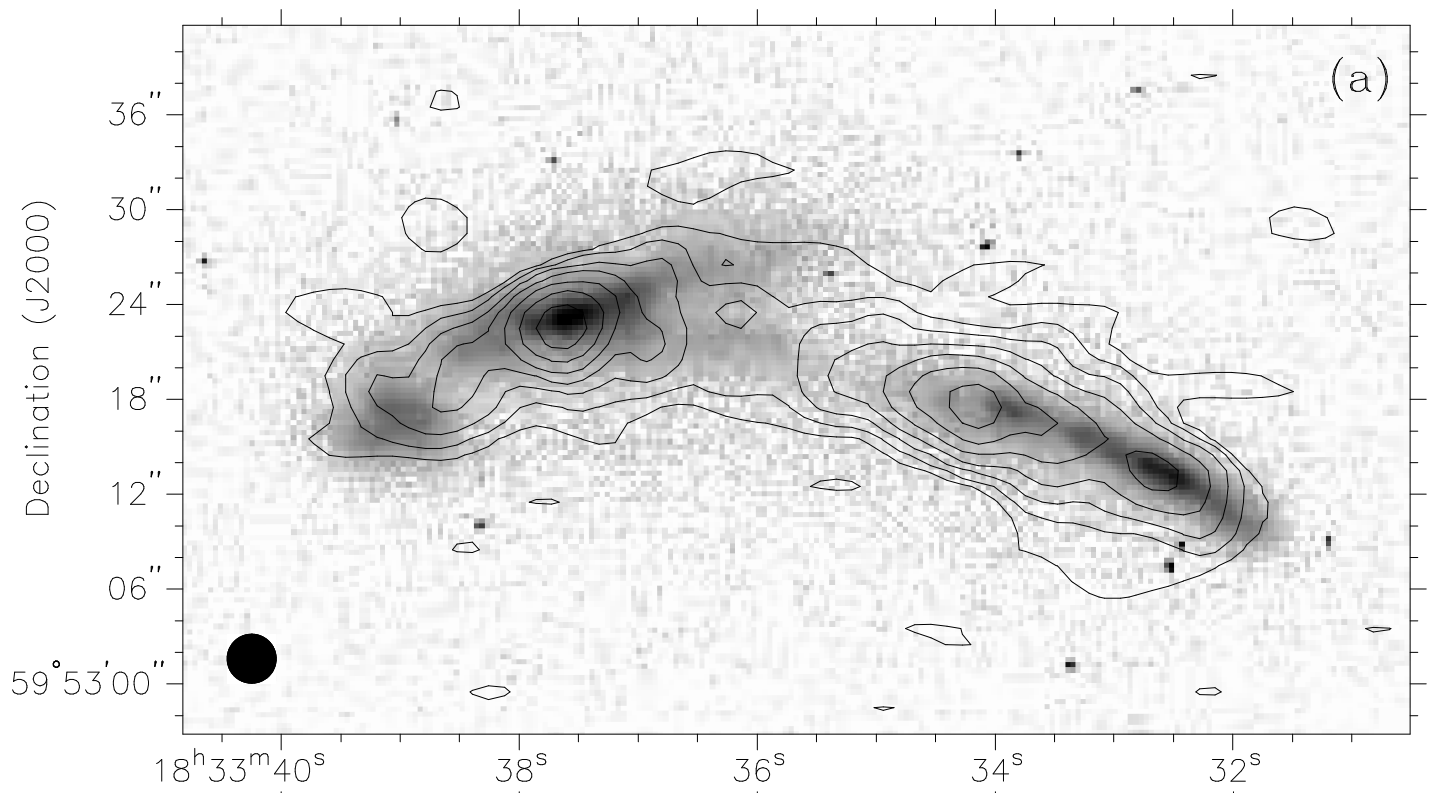


This figure "fig9.jpg" is available in "jpg" format from:

<http://arxiv.org/ps/astro-ph/0103280v1>

This figure "fig10.jpg" is available in "jpg" format from:

<http://arxiv.org/ps/astro-ph/0103280v1>





This figure "fig12.jpg" is available in "jpg" format from:

<http://arxiv.org/ps/astro-ph/0103280v1>

This figure "fig13.jpg" is available in "jpg" format from:

<http://arxiv.org/ps/astro-ph/0103280v1>